Large-amplitude coastal shelf waves

Andrew L. Stewart,[1] Paul J. Dellar,[2] and Edward R. Johnson[3]

Abstract. Coastal currents typically flow parallel to the continental shelf break, which separates the shallow coastal waters from the open ocean. Decades of theoretical and numerical studies have elucidated the dynamics over continental shelves, but laboratory experiments have tended to focus either on topographic Rossby shelf waves or on narrow, buoyant coastal currents. In this chapter we review these previous studies and describe experiments in which large-amplitude shelf waves are generated by a broad, barotropic, retrograde coastal current in the lee of a continental headland. We discuss an approximate nonlinear wave theory for this configuration and evaluate the experiments quantitatively using numerical solutions of the shallow water-quasigeostrophic equations. A consistent feature that emerges in our numerical solutions and experiments is that large-amplitude shelf waves rapidly steepen and break. The characteristics of the wave breaking are poorly described by nonlinear wave theory, but are quantitatively well-captured by our numerical modelling.

1. Shelf waves and coastal currents in the laboratory

Coastal currents flowing along continental shelves are a complex dynamical feature of the global ocean. Such currents separate the coastal waters from the open ocean, and so control the transport of both dynamical and passive tracers across and along the continental slope [*Nittrouer and Wright*, 1994]. Some of the most climatically important currents in the world ocean flow partly or entirely as shelf currents, so understanding their behaviour represents an important oceanographic and dynamical problem. For example, the Antarctic Slope Front (ASF) [*Thompson and Heywood*, 2008] mediates transport of Continental Deep Water onto the Antarctic continental shelf. This is responsible for preserving biological primary production around the Antarctic margins [*Prézelin et al.*, 2004], and controls the melting rate of ice shelves [*Martinson et al.*, 2008]. The Agulhas current, which flows over the continental shelf in the Mozambique Channel [*Bryden et al.*, 2005; *Beal et al.*, 2006, 2011], facilitates mass and heat exchange between the Indian and Atlantic oceans via thermocline water transported in Agulhas eddies [*Gordon*, 1985, 1986]. The Gulf Stream flows along the coastal shelf of North America until it separates at Cape Hatteras [*Stommel*, 1972; *Johns and Watts*, 1986; *Pickart*, 1995]. This current is associated with large meridional heat transport, and closes the upper branch of the Atlantic Meridional Overturning Circulation [*Minobe et al.*, 2008].

The sharp increase in depth at the continental shelf break exerts a strong constraint on the flow via conservation of potential vorticity (PV) [see *Pedlosky*, 1987; *Vallis*, 2006]. This motivates a description of the flow in terms of topographic Rossby waves. *Longuet-Higgins* [1968] first showed that a continental shelf acts as a wave-guide, approximating the bathymetry as a discontinuity in depth. Shelf wave theory was subsequently adapted to a wide range of bathymetric configurations and applied to regions of the real ocean [*Mysak*, 1980b, a]. For example, *Mysak et al.* [1979] applied linear wave theory applied to double-exponential approximations of coastal depth profiles in the Pacific ocean, whilst *Gill and Schumann* [1979] attempted to predict the path of Agulhas using an idealized representation of continental slope and deep ocean in a two-layer model. Linear shelf wave theory has since been extended to describe more realistic configurations such as continental shelves with alongshore depth variations [*Johnson*, 1985; *Johnson and Davey*, 1990], curved coastlines [*Kaoullas and Johnson*, 2010; *Johnson et al.*, 2012], and arbitrary isobath variations [*Rodney and Johnson*, 2012; *Kaoullas and Johnson*, 2012].

Coastal currents complicate this Rossby wave description of shelf dynamics, particularly when they flow over alongshore variations in the bathymetry, and when they are driven by a time-dependent inflow or wind stress [*Allen*, 1980; *Brink*, 1991]. The development of numerical ocean models, particularly those adapted to large variations in bathymetry [*e.g. Haidvogel et al.*, 2008], has advanced our understanding of such situations considerably in recent decades. Yet laboratory studies of coastal dynamics have tended to focus either on topographic Rossby wave propagation or on coastal current evolution, so in this section we review separate selections of previous studies along each line of investigation. Both provide context for the experiments that serve as the focus of this chapter, which describe the evolution of a coastal current in terms of large-amplitude shelf waves.

1.1. Shelf waves

Ibbetson and Phillips [1967] performed some of the earliest laboratory experiments relevant to Rossby shelf wave dynamics. They constructed a rotating annulus between radii of 72.4 cm and 102.0 cm, similar to that described in §2. A background PV gradient was provided simply by the curvature of the free surface, required to balance the centrifugal force. Rossby waves were generated by the oscillatory rotation of a vertical paddle positioned across the breadth of the channel, with periods between 20 and 100 seconds. In an open annulus the damping rate of the resulting Rossby waves was found to be of the same order of magnitude as the theoretical prediction (see §3.1). When a 60°

[1]Environmental Sciences and Engineering, California Institute of Technology, Pasadena, California, USA.
[2]Oxford Centre for Industrial and Applied Mathematics, University of Oxford, Oxford, England, UK.
[3]Department of Mathematics, University College London, London, England, UK.

Accepted for publication in 'Modelling atmospheric and oceanic flows: insights from laboratory experiments and numerical simulations', Geophysical Monograph Series.

arc of the annulus adjacent to the paddle was enclosed, the waves intensified at the far boundary, equivalent to western boundary intensification in the real ocean.

Caldwell et al. [1972] performed the first experiments that directly represented the continental slope and deep ocean. They constructed an annular channel in which the fluid depth increased exponentially with radius over the inner half of its width, and remained constant over the outer half, following the theoretical approximation of *Buchwald and Adams* [1968]. Rossby shelf waves were generated via one or two radially-oscillating paddles, and visualized via aluminium tracer particles and streak photography. The measured dispersion relation for the waves was found to agree closely with the linear theory of *Buchwald and Adams* [1968]. *Caldwell and Eide* [1976] used a similar set-up to study Rossby waves over a shelf whose depth increased linearly with radius, and Kelvin waves in a channel of uniform depth. Both were found to agree well with theoretical predictions once the assumption of a non-divergent horizontal velocity field was relaxed [*Buchwald and Melville*, 1977].

Colin de Verdiere [1979] examined Rossby wave-driven mean flows in a rotating cylinder of radius 31 cm. The curvature of the fluid's free surface supplied a background vorticity gradient, and an array of sources and sinks was used to excite a travelling wave with azimuthal wavenumber 12. The Rossby waves were found to generate a strong mean flow along planetary vorticity contours, equivalent to isobaths on a continental shelf. *Sommeria et al.* [1991] performed similar experiments in an annular channel between radii of 21.6 cm and 86.4 cm, with a depth that increased linearly with radius. Forcing was again supplied by an inner ring of sources and an outer ring of sinks, or *vice versa*, in the floor of the channel. The resulting net radial transport drove an azimuthal jet via the Coriolis force, whose direction was dictated by the relative radii of the sources and sinks. The jet supported unstable Rossby waves with azimuthal wavenumbers ranging from 3 to 8.

Pierini et al. [2002] analysed Rossby normal modes over a 2 m-wide experimental slope connecting water depths of 30 cm and 60 cm. The slope was confined by walls to a finite length of 4.3 m or 3.3 m, and the tank was rotated with periods ranging from 30 s to 50 s. A paddle was used to drive deep fluid gradually and barotropically onto the slope, where it excited Rossby normal modes between the walls confining the slope. The phases of these modes agreed well with numerical solutions of a barotropic shallow water model, but their amplitudes exhibited some substantial discrepancies.

Most recently, *Cohen et al.* [2010] generated topographic Rossby waves in an experimental slope configuration similar to that of *Caldwell et al.* [1972]. They constructed an annular channel between radii of 1 m and 6.5 m, with a fluid whose depth was uniform in the innermost 1.5 m and decreased linearly by 0.4 m over the outermost 4 m. Shelf waves were excited by a radially-oscillating paddle of length 2 m or 0.4 m. The resulting wave velocities were measured using particle imaging velocimetry. The dispersion relation and radial velocity of the experimentally-generated waves was found to agree closely with a theory derived from the linearized barotropic shallow water equations. *Cohen et al.* [2012] performed similar experiments in an annular channel between radii of 0.25 m and 1 m, with linear decrease in the depth from the center to zero at the outer edge. Topographic waves were generated via three radially-aligned paddles, and compared with linearized shallow water theory. Approximating the continental boundary as a vertical wall, rather than a vanishing ocean depth, was found to distort the frequencies in the wave dispersion relation, resulting in disagreement with the experimental results.

1.2. Coastal currents

Even the simplest representation of a coastal current flowing along a continental slope requires a more sophisticated treatment in the laboratory than topographic Rossby waves, and a much smaller body of analytical theory exists to predict their behaviour. As a result, laboratory studies of coastal currents followed two decades after the first experiments with topographic Rossby waves. *Whitehead and Chapman* [1986] performed the first such study, generating a coastal current by attaching a rectilinear slope to the outside of a cylindrical tank. A buoyant gravity current was released at the outer edge of the tank, then propagated around the edge of the tank and the along the slope. The gravity current was found widen to reduce its speed by a factor of up to 4 upon reaching the slope. If the current's speed fell below that of the first barotropic linear topographic wave then it would radiate energy forward along the slope as a shelf wave.

Cenedese and Linden [2002] advanced this approach by constructing an annular channel between radii of 13 cm and 43 cm, with four axisymmetric topographic configurations: a flat bottom, a step, a raised shelf with a slope, and a raised step with a slope. Buoyant fluid was injected via an axisymmetric source at the inner wall of the annulus, forming a symmetric coastal current that was eventually subject to baroclinic instability. Introducing a shelf produced instabilities with slightly higher azimuthal wavenumbers, and resulted in secondary instability after axisymmetry was re-established.

Cenedese et al. [2005] constructed a coastal geometry qualitatively similar to that discussed in §2, but in a rectilinear channel. An experimental slope of width 4 cm and height 6 cm separated a shelf from the deep ocean, each of width 40cm. The channel was 84 cm long and bounded at each end by vertical walls, one of which was used to steer a baroclinic jet towards the slope. The experimental results agreed qualitatively with the quasigeostrophic (QG) theory of *Carnevale et al.* [1999]: the jet either split between the tank edge and the slope, or retroflected away from the slope.

Folkard and Davies [2001] were the first to investigate along-slope variations in the experimental topography, a crucial element of the experiments discussed in §2. They employed a rectangular channel with a linear slope that was broken by a gap of varying length, filled with linearly-stratified fluid. They then introduced a gravity current at one end of the channel, hugging either the slope or the "continental" channel wall. Breaking the slope was found to slow and destabilize the current, leading in some situations to the formation of persistent eddies at the upstream end of the gap. *Wolfe and Cenedese* [2006] employed a very similar experimental configuration, and observed the same behaviour in buoyant coastal currents with a gap in the slope. They also introduced slopes of various steepness in the gap, and found that the current was stabilized whenever it width was smaller than that of the slope.

Sutherland and Cenedese [2009] extended this approach to a more realistically-shaped trough in the experimental shelf. This configuration is conceptually opposite to the experiments described in §2, which represent a headland projecting out from the continent. Their experimental set-up closely resembled that of *Whitehead and Chapman* [1986]: a buoyant coastal current was injected at one side of a cylindrical tank, and then flowed around its edge until it encountered a rectilinear slope of height 20 cm and breadth ~ 30 cm. The slope was interrupted for around 25 cm by a canyon of length ~ 30 cm. The coastal current would separate from the bathymetry to cross the canyon if the width of the flow exceeded the radius of curvature of the isobaths, in some cases forming a counter-rotating eddy in the canyon itself.

1.3. Large-amplitude shelf waves

The theoretical and experimental studies of shelf waves described above focus almost exclusively on linear dynamics,

for which a developed body of literature exists [*e.g. Mysak*, 1980b]. Yet in experiments featuring coastal currents, the evolution is characterized by strongly nonlinear features, such as the generation of eddies and large-amplitude deviations of the streamlines away from the isobaths [*e.g. Sutherland and Cenedese*, 2009].

In fact a description of coastal currents in terms of nonlinear Rossby shelf waves is possible, but requires that the shelf break is approximated as a discontinuity in depth [*Longuet-Higgins*, 1968], and that the wave is long and evolves slowly in time. Under these assumptions *Haynes et al.* [1993] derived a nonlinear wave equation, based on a solution of the QG equations in the limit of long wavelength. *Clarke and Johnson* [1999] and *Johnson and Clarke* [1999] extended this solution to first order under an asymptotic expansion, and thereby derived a dispersive correction to the wave equation. *Johnson and Clarke* [2001] summarised the development and application of this theory.

This chapter focuses on experiments that are amenable to exactly this kind of theoretical description. We consider a channel similar to that of *Cenedese et al.* [2005], with a narrow slope separating much broader shallow and deep regions representing the continental shelf and open ocean respectively. This is illustrated schematically in Figure 1. Our experiments elucidate the dynamics of a retrograde coastal current flowing past a headland, where the continental wall of the channel protrudes out, narrowing the continental shelf. Examples of such a configuration in the real ocean include the Agulhas current in the Mozambique Channel [*Bryden et al.*, 2005; *Beal et al.*, 2006, 2011], and the Gulf Stream at Cape Hatteras [*Stommel*, 1972; *Johns and Watts*, 1986; *Pickart*, 1995].

In §2 we describe our experimental set-up and procedure, and characterize the evolution of large-amplitude waves generated by retrograde flow past a headland . In §3 we briefly review the QG equations that underlie our nonlinear wave theory and numerical simulations. In §4 we adapt nonlinear shelf wave theory [*Johnson and Clarke*, 2001] to the annular channel, and in §5 we describe our numerical scheme for the QG equations. In §6 we compare the skill of our theory, numerical solutions, and experiments in predicting the characteristics of large-amplitude wave breaking. Finally, in §7 we summarise our findings and relate our results to previous studies of topographic Rossby waves and coastal currents.

2. Experiments with large-amplitude shelf waves

The purpose of our laboratory experiments is to capture the key features of continental shelves that are separated from the deep ocean by a relatively narrow slope. This configuration permits topographic Rossby waves whose amplitudes are large compared to the width of the slope; our goal is to elucidate the nonlinear dynamics of these waves. In this section we detail the set-up of our experiments, and illustrate their behaviour via a reference experiment that characterizes our results.

In the laboratory, creating a straight, extended coastline with a flowing coastal current that is subject to a Coriolis force is logistically difficult. We therefore represent an idealized coastal ocean using a channel around the circumference of a rotating cylindrical tank, shown schematically in Figure 1. A retrograde coastal current of uniform density flows between rigid walls at $r = R_w$ and $r = R_c$, representing the oceanward extent of the current and the continental landmass respectively. The flow is confined beneath a rigid lid at $z = H$, and above an ocean bed whose height ranges from 0 at $r = R_w$ to H_s at $r = R_c$ via a narrow slope of width W_s at $r = R_h$. This configuration also serves as the basis of the QG theory described in §3–5.

We conducted all of our experiments in a cylindrical tank of radius $R_c = 1.065\,\mathrm{m}$, shown in Figure 2. We constructed

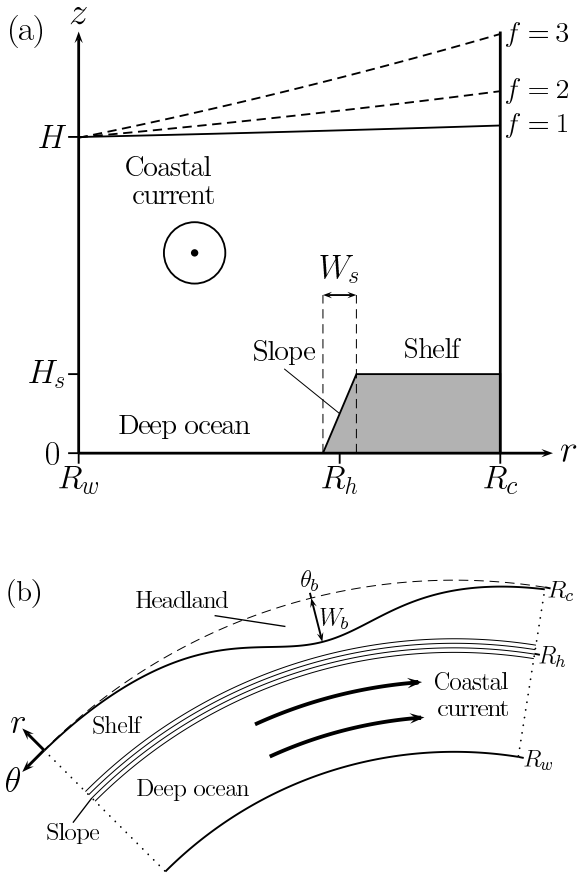

Figure 1. The idealized coastal ocean represented in our laboratory experiments and QG theory.

an inner wall of radius $R_w = 0.75\,\mathrm{m}$ using a Plexiglas sheet weighted to the floor of the tank, leaving an annular channel of width $L = 31.5\,\mathrm{cm}$. We built a flat shelf of width 10.75 cm and height $H_s = 5\,\mathrm{cm}$ around the outer edge of the tank, and attached a uniform slope of width $W_s = 2.5\,\mathrm{cm}$. The radius of the slope center is therefore $R_h = 0.945\,\mathrm{m}$. We painted the entire tank floor, shelf and slope to ensure uniform bottom surface properties, as we found that bottom friction was by far the dominant source of dissipation in the experiments. The tank was filled with fresh water of uniform temperature to a depth $H = 20\,\mathrm{cm}$ prior to each experiment.

This configuration differs from that of the real ocean in several respects:

1. The curvature of the channel influences the propagation of waves due to the radial dependence of any azimuthal volume element (see §4). We minimize this influence by using a channel whose width L is much smaller than the tank radius R_c.

2. In solid-body rotation, the upper surface of the fluid curves up toward the outer edge of the tank to balance the centrifugal force, as shown in Figure 1. The variation of the surface height across the channel is reaches 6.6 cm when $f = 3\,\mathrm{rad\,s^{-1}}$, exceeding the 5 cm drop in depth across the experimental slope. However, even in this case the experimental slope is around ten times steeper than the free surface, and thus remains the dominant source of relative vorticity.

3. Real coastal currents are not bounded offshore by a wall, but rather by the open ocean. However, the wall at $r = R_w$ is necessary to prevent the current interacting with itself across the tank, a situation that is more appropriate to

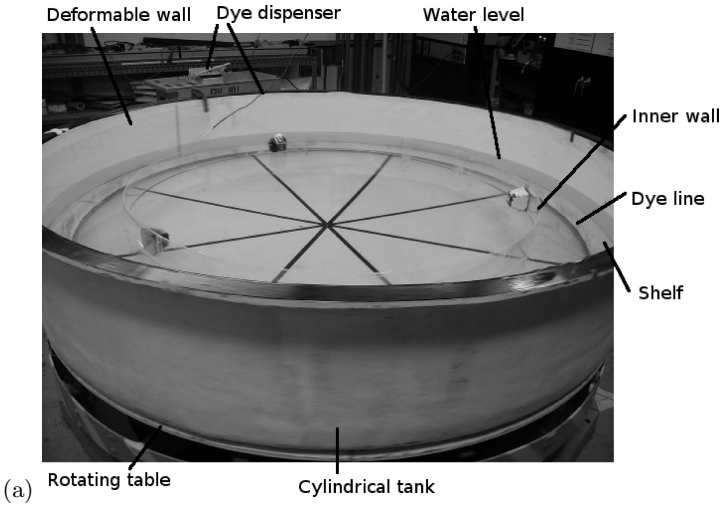

(a) (b)

Figure 2. (a) An illustrative photograph of the rotating tank, with elements of the experimental labeled, and (b) a photograph of our reference experiment from the overhead camera. We photographed (a) before attaching the experimental slope in order to distinguish the shelf, and also before the base of the tank was repainted for the experiments.

a lake or small sea [*e.g. Johnson*, 1987; *Johnson and Kaoullas*, 2011].

4. The depths of continental shelves in the real ocean tend to be small compared to the full ocean depth. We used a relatively deep experimental shelf because we found that very shallow flows were damped too quickly by bottom friction. Furthermore, a small shelf is amenable to analysis using QG theory, for which a body of literature already exists [see *Johnson and Clarke*, 2001]. These studies have demonstrated that the vortical dynamics captured by QG theory are most important for understanding shelf waves, and that the mass constraints imposed by a shallow shelf are secondary. The relevance of two-dimensional experimental flows over topography to real geophysical flows is discussed at length in Chapter 10 of this volume.

5. Our experiments omit variations in density, which are dynamically important throughout the ocean. However, the barotropic dynamics are still informative, and strongly barotropic velocity profiles have been observed in the Agulhas current [*Bryden et al.*, 2005; *Beal et al.*, 2006].

All of the results described below concern shelf waves generated in the lee of a continental headland that protrudes out onto the continental shelf. In the laboratory we constructed a bump by attaching a sheet of plexi-glass to the outer wall of the tank, and then forcing its center out onto the shelf by placing a wedge behind it. This apparatus is visible in Figure 2. The outer wall of the channel is therefore given by $r = R_b(\theta)$. The bump in our annular channel, which was held fixed in all of the experiments below, is accurately described by

$$R_b = R_c - W_b(\theta), \quad W_b(\theta) = W_{b0}\,\mathrm{sech}^2\left(\frac{\theta-\theta_b}{\Theta_b}\right), \qquad (1)$$

where $W_{b0} = 8.3\,\mathrm{cm}$, $\theta_b = 1.82\,\mathrm{rad}$ and $\Theta_b = 0.18\,\mathrm{rad}$. At the maximum extent of the protrusion, the width of the experimental shelf is reduced to 3.5 cm. This shape has been chosen to produce long waves with large amplitudes, which may be expected to exhibit nonlinear behaviour without breaking.

In each experiment, we rotate the tank at a constant rate until the water within is brought to rest in the rotating frame. We then inject a line of dye into the fluid surface over the center of the slope, at the PV front. This dye line serves as a passive tracer, intended to track the PV front as it is advected around the channel. We track the evolution of the dye line using an overhead camera that co-rotates with the tank, producing images like those shown in Figure 3. We generate a mean flow, representing along-shore transport by a coastal current, by rapidly changing the Coriolis parameter of the tank from $f - \Delta_f$ to f. This imparts a relative vorticity of $-\Delta_f$ to all of the water in the tank, inducing an azimuthal flow with sign opposite to that of Δ_f. For all of the experiments described herein we use $\Delta_f > 0$, yielding a retrograde coastal current. We found that a retrograde current would develop large-amplitude shelf waves in the lee of the coastal protrusion, whereas a prograde current would not. This phenomenon may be understood via the nonlinear shelf wave theory described in §4. *Clarke and Johnson* [1999] showed that waves with the smallest amplitudes have the largest phase speeds unless the shelf line lies very close to one of the channel walls. Thus, disturbances formed by a prograde coastal current propagate rapidly downstream as small-amplitude waves, preventing a large wave envelope from forming on the continental shelf.

We have performed experiments over a range of tank rotation rates $f \in \{1, 1.5, 2, 2.5, 3\}\,\mathrm{rad\,s^{-1}}$, and coastal current speeds corresponding to $\Delta_f \in \{0.01, 0.02, \ldots, 0.07\}\,\mathrm{rad\,s^{-1}}$. For the purpose of illustration, we define a reference experiment with $f = 1.5\,\mathrm{rad\,s^{-1}}$ and $\Delta f = 0.03\,\mathrm{rad\,s^{-1}}$ that characterizes the evolution of the shelf waves generated by our coastal current. Figure 3 shows images of the dye line close to the coastal protrusion at several times in this experiment. Between $t = 0\,\mathrm{s}$ and $t = 17\,\mathrm{s}$, the coastal current advects fluid past the protrusion, developing a long wave with large amplitude. The rear portion of the wave then steepens continually until $t = 29\,\mathrm{s}$, at which point the dye is aligned radially. By $t = 45\,\mathrm{s}$ the wave has over-steepened and broken, and the position of the dye-line is a double-valued function of azimuth. Thereafter, as the vorticity in the over-steepened wave envelope is removed by bottom friction, it gradually unwinds in the mean flow, forming an undulating wave train by $t = 66\,\mathrm{s}$. Eventually both sides of this wave train curl up on themselves, as shown at $t = 104\,\mathrm{s}$. In the following sections we will interpret this behaviour using an adaptation of nonlinear shelf wave theory to the annulus, and using numerical simulations of the barotropic QG shallow water equations.

3. Quasigeostrophic model equations

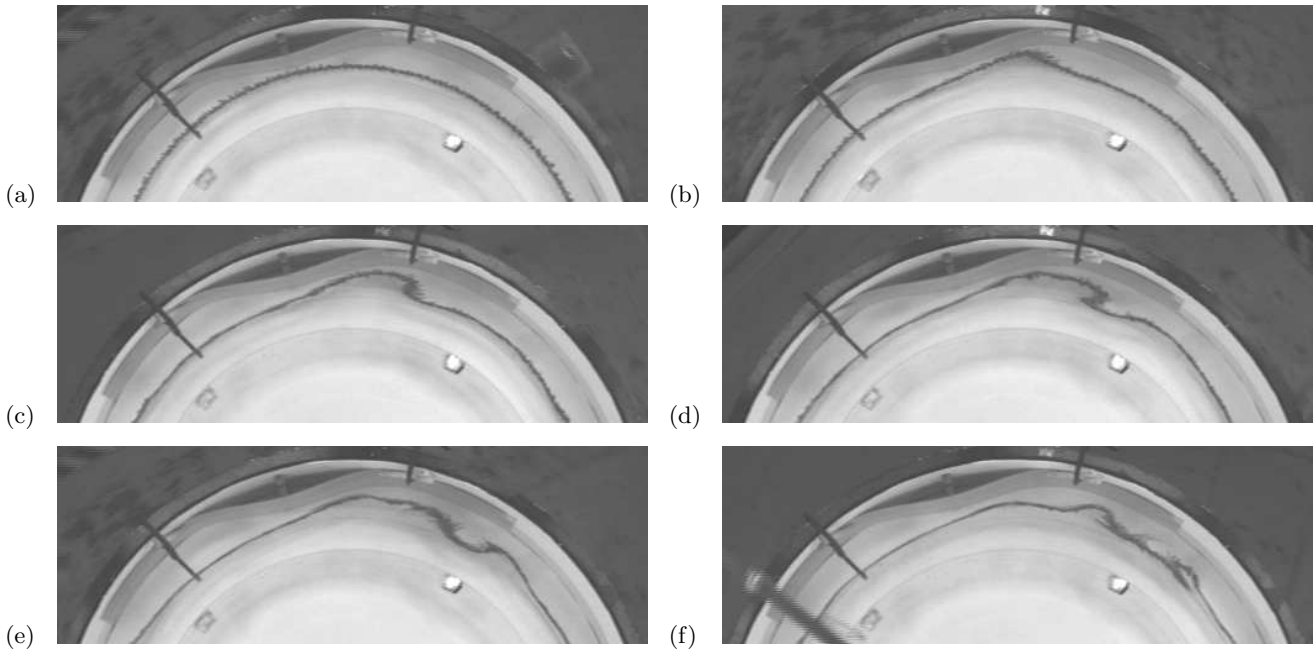

Figure 3. Snapshots from our reference experiment at (a) $t = 0\,\mathrm{s}$, (b) $t = 17\,\mathrm{s}$, (c) $t = 29\,\mathrm{s}$, (d) $t = 45\,\mathrm{s}$, (e) $t = 66\,\mathrm{s}$, and (f) $t = 104\,\mathrm{s}$.

We model the flow in our annular channel using the shallow water–QG equations [*Pedlosky*, 1987; *Vallis*, 2006]. The single-layer shallow water equations describe the evolution of a homogeneous layer of fluid, under the assumption that the flow is restricted to columnar motion and confined beneath a rigid lid at its upper surface. This assumption is consistent with a small ratio of vertical to horizontal lengthscales, $H/L \ll 1$, and appropriate for motions much slower than the surface gravity wave speed. The QG equations are derived thereafter by posing an asymptotic expansion for a small Rossby number, $\mathrm{Ro} = U/fL \ll 1$ where U and L are characteristic horizontal velocity and length scales respectively. Variations of the bottom topography h/H are also assumed to be $\mathcal{O}(\mathrm{Ro})$.

For the configuration shown in Figure 1 we define the horizontal lengthscale as $L = R_c - R_w$ and the velocity scale as $U = \frac{1}{2}\left|\Delta_f\right| R_h$, so $L = 31.5\,\mathrm{cm}$ and $U \approx 1.4\,\mathrm{cm\,s^{-1}}$. These scales yield an aspect ratio of $H/L \approx 0.6$ and a Rossby number of $\mathrm{Ro} \approx 0.03$, whilst the variations of the bottom topography are characterized by $H_s/H = 0.25$. Whilst these quantities are all smaller than 1, they are large enough to call QG theory into question. In practice, however, the rotation of the tank is sufficiently strong that the fluid adheres closely to columnar motion, due to the Taylor-Proudman effect. *Williams et al.* [2010] showed that this theory provides qualitatively accurate results for rapidly rotating flows that are far outwith the formal QG regime.

3.1. Interior dynamics

Under the assumptions of shallow water QG theory, the conservation of horizontal fluid momentum in our annular channel may be expressed in the form,

$$\frac{\partial \boldsymbol{u}}{\partial t} + q\hat{\boldsymbol{e}}_z \times \boldsymbol{u} + \nabla\left[\Pi + \tfrac{1}{2}\left|\boldsymbol{u}\right|^2 - \Psi\right] = -\kappa \boldsymbol{u}, \qquad (2)$$

where $\boldsymbol{u} = -\nabla \times \psi \hat{\boldsymbol{e}}_z = u\hat{\boldsymbol{e}}_r + v\hat{\boldsymbol{e}}_\theta$ is the depth-independent horizontal velocity, and Π is the pressure at the rigid lid $z = H$. The PV is defined as

$$q = \zeta + \frac{fh}{H}, \qquad (3)$$

and we denote the height of the bottom topography as $h(r)$,

$$h(r) = H_s \begin{cases} 0, & r \le R_h - \frac{1}{2}W_s, \\ \dfrac{r + \frac{1}{2}W_s - R_h}{W_s}, & \left|r - R_h\right| \le \frac{1}{2}W_s, \\ 1, & R_h + \frac{1}{2}W_s \le r, \end{cases} \qquad (4)$$

as shown in Figure 1. Finally, Ψ is the first-order transport streamfunction

$$H\boldsymbol{u}_{\mathrm{ag}} - h\boldsymbol{u} = -\nabla \times \Psi \hat{\boldsymbol{e}}_z, \qquad (5)$$

where $\boldsymbol{u}_{\mathrm{ag}}$ is the (unknown) ageostrophic correction to the velocity. Taking the curl of (2) yields a material conservation law for PV, as modified by friction proportional to κ,

$$\frac{\mathrm{D}q}{\mathrm{D}t} = -\kappa\zeta, \qquad \zeta = \nabla^2\psi. \qquad (6)$$

Here $\mathrm{D}/\mathrm{D}t \equiv \partial/\partial t + \boldsymbol{u}\cdot\nabla$ is the advective derivative and ζ is the relative vorticity.

Motivated by our experimental observations, we have neglected any viscous dissipation in (2) because bottom friction removes energy from the flow much more rapidly. The action of bottom friction is represented by a linear drag with the constant rate κ set by QG theory [*Pedlosky*, 1987],

$$\kappa = \sqrt{A_v f}/H. \qquad (7)$$

The vertical viscosity A_v is here simply the molecular viscosity $\nu = 1 \times 10^{-6}\,\mathrm{m^2\,s^{-1}}$. *Ibbetson and Phillips* [1967] found that the damping of Rossby waves in a similarly-sized annulus was accurately described by (7).

We have separately conducted experiments without the bump in the outer wall, in which we release dye along a line of constant azimuth and then reduced f from $1.5\,\mathrm{rad\,s^{-1}}$ to $1.3\,\mathrm{rad\,s^{-1}}$. This bestows upon the fluid a uniform angular velocity that may be expected to decay with an e-folding time of κ^{-1}. We estimate that, off the shelf, κ is around 1.8 times smaller than the theoretical value (7), whilst on the shelf it is around 1.5 times larger than (7). It is not clear

why the variation in κ should be so large; simply replacing H by the actual depth $H-h$ in (7) can not account for this. Nonetheless, (7) is a reasonable approximation to the bottom friction over the whole annulus. However, repeated measurements are not available to provide an accurate parameterization of κ, nor to explain the apparent discrepancy in κ between deeper and shallower waters.

3.2. Initial conditions

As described in §2, we initiate our experiments by changing the tank's Coriolis parameter from $f-\Delta_f$ to f. This acceleration is relatively rapid, requiring only 1–2 s, so for the purposes of our model we treat it as an instantaneous modification of the fluid velocity in the rotating frame between $t=0^-$ and $t=0^+$. This avoids reformulating the QG equations for a frame rotating with variable velocity.

Relinquishing the QG approximation momentarily, we note that at $t=0^-$ the fluid is in solid-body rotation with the tank, and so adheres exactly to columnar motion. The absolute vertical vorticity ζ_a of any fluid column is then equal to that of the tank,

$$\zeta_a|_{t=0^-} = f-\Delta_f. \tag{8}$$

The acceleration of the tank modifies the absolute vorticity of its walls and base, but leaves the absolute vorticity of the fluid instantaneously unchanged. Formally, we require that

$$\zeta_a|_{t=0^+} = f+\zeta|_{t=0^+} = \zeta_a|_{t=0^-}, \tag{9}$$

so our initial condition for the QG relative vorticity is

$$\zeta(r,\theta,0^+) = -\Delta_f. \tag{10}$$

That is, the fluid acquires a relative vorticity that is everywhere equal to the change in the Coriolis parameter. One could follow a similar line of reasoning under the QG approximation, but the small-Rossby number approximation of the PV (3) would introduce an $\mathcal{O}(H_s/H)$ error in (10).

Although (10) provides an initial condition for ζ, and therefore for q, the initial streamfunction $\psi(r,\theta,0^+)$ is not uniquely determined by (10) alone. To invert (6) for ψ at $t=0^+$ we require the streamfunction $\psi_0(0^+)$ on $r=R_b$, which corresponds to the along-channel transport. We obtain ψ_0 under the QG approximation by considering the total kinetic energy of the fluid in an inertial frame,

$$E(t) = \tfrac{1}{2}\iint_A \left\{u^2+(V+v)^2\right\}\mathrm{d}A, \tag{11}$$

where V is the azimuthal velocity due to the rotation of the tank, and A denotes the area of the annulus. In our model, only bottom friction can extract energy from the fluid, and we assume that this may be neglected during the rapid acceleration of the tank. We therefore require conservation of total energy across $t=0$, *i.e.* $E^{(-)}=E^{(+)}$ where

$$E^{(-)} = \tfrac{1}{2}\iint_A \left(\tfrac{1}{2}fr\right)^2 \mathrm{d}A, \tag{12a}$$

$$E^{(+)} = \tfrac{1}{2}\iint_A \left\{u^2+\left(\tfrac{1}{2}\left(f+\Delta_f\right)r+v\right)^2\right\}\mathrm{d}A. \tag{12b}$$

Thus, $\psi_0(0^+)$ must be chosen such that (12a) and (12b) are equal. For example, in a regular annulus ($W_b\equiv 0$), this yields $\psi_0(0^+)=\frac{1}{4}\Delta_f\left(R_c^2-R_w^2\right)$, which corresponds to the intuitive result that the fluid acquires a uniform angular velocity opposite to the direction of the tank's acceleration. In general, $E^{(-)}=E^{(+)}$ must be solved numerically, but the long-wavelength asymptotic analysis described in §4 provides a very accurate approximate solution for the slowly-varying channel shown in Figure 2.

3.3. Boundary conditions

We apply no-flux boundary conditions at the inner and outer walls of the channel, requiring that both be streamlines of ψ. Without loss of generality we choose

$$\psi\left(R_w,\theta,t\right)=0, \qquad \psi\left(R_b,\theta,t\right)=\psi_0(t), \tag{13}$$

so ψ_0 corresponds to the counter-clockwise along-channel transport. In a regular annulus ($W_b\equiv 0$) it is possible to derive an analytical evolution equation for $\psi_0(t)$ that excludes contributions from the unknown lid pressure Π. This is not possible when $W_b\neq 0$, because the bump in the outer wall may support an azimuthal pressure gradient that modifies the along-channel transport ψ_0. Instead we determine additional boundary conditions by considering the circulations Γ_w and Γ_c around the inner and outer walls of the tank respectively [*McWilliams*, 1977]. It follows from (2) that

$$\frac{\mathrm{d}}{\mathrm{d}t}\Gamma_c = -\kappa\Gamma_c, \qquad \Gamma_c = \oint_{r=R_b}\boldsymbol{u}\cdot\mathrm{d}\boldsymbol{r}, \tag{14a}$$

$$\frac{\mathrm{d}}{\mathrm{d}t}\Gamma_w = -\kappa\Gamma_w, \qquad \Gamma_w = \oint_{r=R_w}\boldsymbol{u}\cdot\mathrm{d}\boldsymbol{r}. \tag{14b}$$

In fact we only need to ensure that either (14a) or (14b) is satisfied, because by Stokes' theorem

$$\Gamma_c-\Gamma_w = \iint_A \zeta\,\mathrm{d}A \implies \frac{\mathrm{d}}{\mathrm{d}t}\left(\Gamma_c-\Gamma_w\right) = -\kappa\left(\Gamma_c-\Gamma_w\right). \tag{15}$$

The second equation in (15) follows from integrating (3) over the annulus. Condition (14b) determines the evolution of the outer wall streamfunction $\psi_0(t)$. We outline separate asymptotic and numerical strategies to solve this problem in §4 and §5 respectively.

4. Nonlinear shelf wave theory

In interpreting the results of our laboratory experiments, it is instructive to compare with the predictions of the established nonlinear shelf wave theory, [*Haynes et al.*, 1993; *Clarke and Johnson*, 1999; *Johnson and Clarke*, 1999, 2001]. This theory approximates the experimental/continental slope as a step, equivalent to $W_s\to 0$ in Figure 1, and describes the evolution of a fluid interface that lies initially over the shelf line, corresponding to the dye line in Figure 3. In this section we adapt this approach to an annular channel, improving upon the derivations of *Stewart* [2010] and *Stewart et al.* [2011] to utilize the initial and boundary conditions described in §3.2 and §3.3 respectively.

4.1. Quasigeostrophic dynamics over a step

In the limit of a vanishingly narrow slope ($W_s\to 0$), the height of the bottom topography in our annular channel becomes

$$h = H_s\,\mathcal{H}(r-R_h), \tag{16}$$

where $\mathcal{H}$ denotes the Heaviside step function. Neglecting the influence of bottom friction, the PV q is conserved exactly on fluid columns, and the dynamics may be described completely by the position of the interface that lies initially above the shelf line. With a view to describing waves whose length is much greater than their amplitude, we make the *a priori* assumption that this interface remains a single valued function of azimuth, and so may be denoted $r=R(\theta,t)$. At $t=0$, we have $R(\theta,0)=R_h$ by definition, and from (3) and (10) the initial PV is

$$q(r,\theta,0) = -\Delta_f + Q\,\mathcal{H}(r-R_h), \tag{17}$$

where $Q = fH_s/H$. Thereafter, material conservation of q ensures that there is always a jump in PV at $r = R$,

$$q(r,\theta,t) = -\Delta_f + Q\,\mathcal{H}(r-R). \tag{18}$$

Using (3) and the definition of the relative vorticity (6), this may be rearranged as a Poisson equation for the streamfunction,

$$\nabla^2\psi = Q\left(-\alpha + \mathcal{H}(r-R) - \mathcal{H}(r-R_h)\right), \tag{19}$$

where we define $\alpha = \Delta_f/Q$. Given the position of the interface $r = R$, inverting (19) yields a complete description of the flow in the annulus at any time t, subject to the boundary equations described in §3.3. The evolution of the interface position $R(\theta,t)$ is determined by the requirement that particles on the interface remain on the interface, i.e. $(D/Dt)(r-R) = 0$. This condition may be rewritten as

$$\frac{\partial R}{\partial t} = -\frac{1}{R}\frac{\partial}{\partial\theta}\psi(R(\theta,t),\theta,t). \tag{20}$$

4.2. Asymptotic solution

In general (19) is not analytically tractable, so instead we obtain an asymptotic solution under the assumption of slow variations in azimuth and time. We first nondimensionalize (19) using the channel width $L = R_c - R_w$ as a length scale and Q^{-1} as a time scale,

$$r = L\hat{r}, \quad t = Q^{-1}\hat{t}, \quad q = Q\hat{q}, \quad \psi = QL^2\hat{\psi}. \tag{21}$$

Here hats $\hat{}$ denotes dimensionless variables. We then rescale under the assumption that azimuthal variations are characterized by $2\pi R_h$, the length of the channel at the shelf line. The parameter $\mu = (L/2\pi R_h)^2$, assumed to be asymptotically small, measures the ratio of radial to azimuthal lengthscales. We further assume that the flow evolves on a time scale that is $\mathcal{O}(\mu^{-1/2})$ longer than Q^{-1}, consistent with a velocity scale of QL and a length scale of $2\pi R_h$. This motivates rescaling θ and $\hat{t}$ as

$$\theta = \mu^{-1/2}\phi, \quad \hat{t} = \mu^{-1/2}\tau. \tag{22}$$

Under this scaling, (19) and (20) become

$$\hat{\psi}_{\hat{r}\hat{r}} + \frac{\hat{\psi}_{\hat{r}}}{\hat{r}} + \frac{\mu}{\hat{r}^2}\hat{\psi}_{\phi\phi} = \mathcal{H}\left(r-R\right) - \mathcal{H}\left(r-R_h\right) - \alpha, \tag{23a}$$

$$\frac{\partial\hat{R}}{\partial\tau} = -\frac{1}{\hat{R}}\frac{\partial}{\partial\phi}\psi\left(\hat{R}(\phi,\tau),\phi,\tau\right), \tag{23b}$$

The asymptotic parameter μ does not enter (23b), and only multiplies the azimuthal derivative in (23a).

We proceed by posing an asymptotic expansion of the streamfunction, $\hat{\psi} = \hat{\psi}^{(0)} + \mu\hat{\psi}^{(1)} + \cdots$. We solve (23a) at successive orders in μ, subject to (13) in the form $\hat{\psi}^{(0)} = \hat{\psi}^{(1)} = 0$ on $r = R_w$ and $\hat{\psi}^{(0)} = \hat{\psi}^{(0)}_0(t), \hat{\psi}^{(1)} = \hat{\psi}^{(1)}_0(t)$ on $r = R_b$. For notational simplicity we present the solution in dimensional variables, writing $\psi = \psi^{(0)} + \psi^{(1)} + \cdots$. The leading-order streamfunction is

$$\begin{aligned}\psi^{(0)}/Q &= -\tfrac{1}{4}\alpha(r^2 - R_w^2) + F\ln(r/R_w)\\ &+ \tfrac{1}{4}(r^2 - R^2)\mathcal{H}(r-R) - \tfrac{1}{2}R^2\ln(r/R)\mathcal{H}(r-R)\\ &- \tfrac{1}{4}(r^2 - R_h^2)\mathcal{H}(r-R_h) + \tfrac{1}{2}R_h^2\ln(r/R_h)\mathcal{H}(r-R_h),\end{aligned} \tag{24}$$

where

$$\begin{aligned}F = \frac{1}{\ln(R_b/R_w)}\Big\{&\psi^{(0)}_0/Q + \tfrac{1}{4}\alpha(R_b^2 - R_w^2)\\ &+\tfrac{1}{4}(R^2 - R_h^2) + \tfrac{1}{2}R^2\ln(R_b/R) - \tfrac{1}{2}R_h^2\ln(R_b/R_h)\Big\}.\end{aligned} \tag{25}$$

Substituting (24) and (25) into (20) yields a non-dispersive nonlinear wave equation for $R(\theta,t)$, analogous to that studied by *Haynes et al.* [1993]. Solutions of this equation rapidly form shocks, so following *Clarke and Johnson* [1999] we continue the asymptotic solution to introduce dispersive terms,

$$\begin{aligned}\psi^{(1)}/Q = &-\tfrac{1}{6}F_{\theta\theta}\ln^2(r/R_w) - \tfrac{1}{2}R_\theta^2\ln^2(r/R)\mathcal{H}(r-R)\\ &+ \tfrac{1}{6}(RR_\theta)_\theta\ln^3(r/R)\mathcal{H}(r-R) + G\ln(r/R_w),\end{aligned} \tag{26}$$

where

$$\begin{aligned}G = \frac{1}{\ln(R_b/R_w)}\Big\{&\psi^{(1)}_0/Q + \tfrac{1}{6}F_{\theta\theta}\ln^2(R_b/R_w)\\ &+\tfrac{1}{2}R_\theta^2\ln^2(R_b/R) - \tfrac{1}{6}(RR_\theta)_\theta\ln^3(R_b/R)\Big\}.\end{aligned} \tag{27}$$

Higher-order corrections may be obtained by continuing the asymptotic solution, but the calculus becomes prohibitively complicated. Substituting (24)–(27) into (20) yields the nonlinear shelf wave equation,

$$\begin{aligned}\frac{\partial R}{\partial t} = -\frac{Q}{R}\frac{\partial}{\partial\theta}\Big\{&-\tfrac{1}{4}\alpha(R^2 - R_w^2) + F\ln(R/R_w)\\ &-\tfrac{1}{4}(R^2 - R_h^2)\mathcal{H}(R-R_h) + \tfrac{1}{2}R_h^2\ln(R/R_h)\mathcal{H}(R-R_h)\\ &+\gamma\Big[-\tfrac{1}{6}F_{\theta\theta}\ln^2(R/R_w) + G\ln(R/R_w)\Big]\Big\}.\end{aligned} \tag{28}$$

Here γ is simply a switch for the dispersive terms due to the first-order streamfunction (26). Setting $\gamma = 0$ recovers the leading-order nondispersive wave equation, whilst $\gamma = 1$ yields the full dispersive wave equation.

4.3. Azimuthal transport

The nonlinear shelf wave equation (28) is closed except for the streamfunction $\psi_0 = \psi_0^{(0)} + \psi_0^{(1)}$ on the outer boundary, or equivalently the along-channel transport. We choose to constrain the transport using (14b) because (14a) is complicated by the bump in the outer wall. Under our asymptotic expansion, the streamfunction must satisfy (14b) at every order in μ. In dimensionless variables, for the dissipation-free case $\kappa = 0$, this implies

$$\frac{\mathrm{d}}{\mathrm{d}t}\Gamma_w^{(n)} = 0, \quad \Gamma_w^{(n)} = \int_0^{2\pi}\left.\frac{\partial\psi^{(n)}}{\partial r}\right|_{r=R_w} R_w\,\mathrm{d}\theta, \tag{29}$$

for all $n \in \{0,1,\ldots\}$. Substituting (24) and (26) into (29) yields evolution equations for $\psi_0^{(0)}$ and $\psi_0^{(1)}$ respectively. For example, for $n = 0$ we obtain

$$\frac{\mathrm{d}\psi_0^{(0)}}{\mathrm{d}t} = -Q\,\frac{\displaystyle\int_0^{2\pi}\frac{\ln(R_b/R)}{\ln(R_b/R_w)}RR_t\,\mathrm{d}\theta}{\displaystyle\int_0^{2\pi}\frac{\mathrm{d}\theta}{\ln(R_b/R_w)}}. \tag{30}$$

We omit the corresponding expression for $\psi^{(1)}$ for the sake of brevity. Equation (30) describes the tendency of net radial vorticity fluxes to modify the along-channel transport. It is

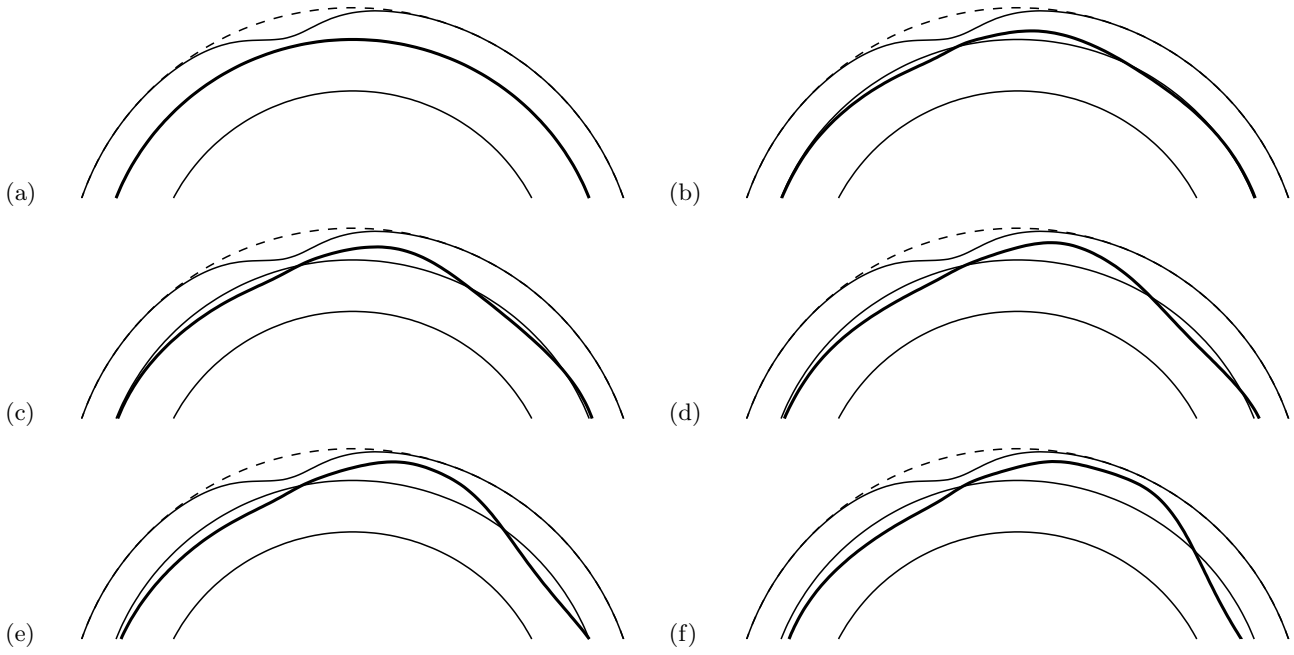

Figure 4. Solution of the nonlinear shelf wave equation (28) using parameters that correspond our reference experiment shown in Figure 3. The thin solid lines show the positions of the inner and outer walls of the annulus, whilst the dashed line indicates the width of the protrusion. The thick solid line indicates the position of the PV front at (a) $t = 0\,\mathrm{s}$, (b) $t = 17\,\mathrm{s}$, (c) $t = 29\,\mathrm{s}$, (d) $t = 45\,\mathrm{s}$, (e) $t = 66\,\mathrm{s}$, and (f) $t = 104\,\mathrm{s}$.

a consequence of our channel's finite length that the wave equation (28) acquires contributions that are dependent on the global behaviour of the solution, whereas that of *Clarke and Johnson* [1999] in an infinite channel did not.

To complete the evolution of $\psi_0(t)$, we must also determine its initial condition following §3.2. Using $R(\theta, 0) = R_h$, equation (24) approximates the initial azimuthal velocity as

$$\left.\frac{\partial \psi^{(0)}}{\partial r}\right|_{t=0} = -\tfrac{1}{2}\Delta_f r + \frac{\psi_0^{(0)}(0) + \tfrac{1}{4}\Delta_f (R_b^2 - R_w^2)}{r \ln(R_b/R_w)}. \quad (31)$$

To a consistent order of approximation, we must omit the radial velocity (u^2) term in (12b), so the initial energy of the flow is

$$E^{(+)} = \tfrac{1}{2} \iint_A \left(\tfrac{1}{2}(f + \Delta_f) r + \left.\frac{\partial \psi^{(0)}}{\partial r}\right|_{t=0} \right)^2 \mathrm{d}A. \quad (32)$$

Thus we may determine $\psi_0^{(0)}(0)$ by substituting (31) into (32) and solving $E^{(+)} = E^{(-)}$. For example, in a regular annulus with $R_b(\theta) \equiv R_c$, equation (31) gives the exact initial streamfunction ($\psi^{(0)}|_{t=0} \equiv \psi|_{t=0}$), and this procedure yields $\psi_0(0) = -\frac{1}{4}\Delta_f (R_c^2 - R_w^2)$. The corresponding azimuthal velocity $v|_{t=0} = -\frac{1}{2}\Delta_f r$ has uniform angular velocity, which is the expected response of the flow to a change in the tank's rotation rate.

4.4. Parameterizing bottom friction

Our neglect of bottom friction in (28) causes its solutions to diverge substantially from our experimental results. It is not possible to introduce κ exactly in our nonlinear wave theory because the vorticity of each fluid column depends sensitively on the times at which it has crossed the shelf line [*Stewart*, 2010]. Instead, we employ a crude representation of bottom friction to provide a source of dissipation in (28). We modify the PV equation (6) to an exact material conservation law,

$$\frac{\mathrm{D}}{\mathrm{D}t}\left(\zeta e^{\kappa t} + \frac{f H_s}{H} \right) = 0. \quad (33)$$

This representation possesses identical conservation laws to (6) and (2) for the total vorticity and total energy in the annulus. In fact, its dynamics are identical to (6) away from the shelf line, where vorticity simply decays exponentially with rate κ. Fluid columns crossing the shelf line acquire a relative vorticity of constant magnitude $|Q|$ under (6), whereas under (33) they acquire a relative vorticity of magnitude $|Q|e^{-\kappa t}$.

All of the results discussed in this section may be rederived using (33). The nonlinear shelf wave equation acquires an additional factor of $e^{-\kappa t}$ multiplying the right-hand side of (28), whilst the azimuthal transport equation (30) is unchanged. The latter may seem contradictory, as the azimuthal transport must decay due to bottom friction. This is because ψ is a streamfunction for the modified vorticity $\zeta e^{\kappa t}$, and so ψ_0 differs from the true along-channel transport by a factor of $e^{-\kappa t}$.

4.5. Comparison with experimental flows

In Figure 4 we plot snapshots of a solution to (28) using parameters that correspond to the reference experiment shown in Figure 3. We solve (28) numerically by discretizing R on an azimuthal grid of 400 equally-spaced points covering $\theta \in [0, 2\pi)$. We evaluate azimuthal derivatives spectrally via the fast Fourier transform, and we integrate (28) forward in time using third-order Adams–Bashforth time-stepping. We employ an exponential Fourier filter [*Hou and Li*, 2007] to damp the mild instability that arises at high wave numbers due to aliasing error [*Boyd*, 2001].

Having assumed that the PV front remains a single-valued function of θ, it is perhaps unsurprising that the solution shown in Figure 4 is unable to capture the wave breaking shown in Figure 3. A large-amplitude wave develops in the lee of the bump in the outer wall, but instead

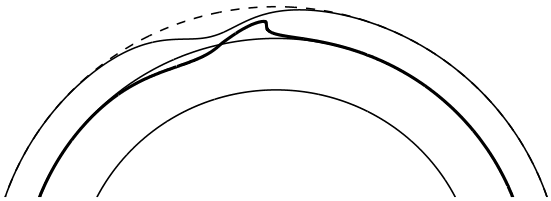

Figure 5. Solution at $t = 8.7\,\mathrm{s}$ of the nondispersive wave equation, corresponding to $\gamma = 0$ in (28), using parameters appropriate to our reference experiment.

of breaking it develops a dispersive wave train that spreads clockwise around the tank due to the strong retrograde mean flow. Although the mean flow decelerates rapidly due to bottom friction, the volume of water transported across the shelf line continues to increase even at $t = 104\,\mathrm{s}$, and the wave envelope does not collapse as in Figure 3.

The wave breaking shown in Figure 3(c) is actually captured more accurately by the nondispersive wave equation, corresponding to $\gamma = 0$ in (28), even though this is formally a less accurate approximation. Figure 5 shows the computed solution to this equation on a grid of 7200 points in azimuth at $t = 8.7\,\mathrm{s}$, around which time the interface $R(\theta, t)$ forms a shock. This solution resembles the experimental wave shown in Figure 3(c), but the wave breaking takes place much earlier in the evolution of the PV front. This may be due to the approximation of the slope as a step, which leads to a larger mean relative vorticity within the theoretical wave envelope.

5. Numerical solution of the inviscid quasigeostrophic equations

In this section we outline our algorithm for solving the QG model equations numerically. This approach is motivated in part by the apparent failure of the long-wave approximation employed in §4 to describe the behaviour of our laboratory experiments. Additionally, these numerical solutions allow us to identify and explain deviations of the experimental results from QG theory, and thus extrapolate to the behaviour of coastal currents in the real ocean.

To ensure stability, we modify the QG model equations (6) to include a numerical viscosity term that smooths vorticity gradients at the scale of the numerical grid,

$$\frac{\partial q}{\partial t} = -J(\psi, q) - \kappa\zeta + A_n \nabla^2 \zeta, \tag{34a}$$

$$\nabla^2 \psi = q - \frac{fh}{H}. \tag{34b}$$

Here J is the two-dimensional Jacobian operator, q and ζ are related via (3), and A_n measures the numerical viscosity. We set $A_n = Qd^2$ so that numerical diffusion becomes comparable to advection at the scale of one grid box d over a dynamical time scale of Q^{-1}. Thus A_n is a purely numerical contribution to (34a), because $A_n \to 0$ as $d \to 0$. The numerical viscosity is not intended to represent the fluid's molecular viscosity, and (34a)–(34b) describe inviscid flow with numerical diffusion that acts only on the interior vorticity field. We therefore retain no-flux, rather than no-slip, boundary conditions at the channel walls.

5.1. Wall-following coordinates

The protrusion (1) in the outer wall of our annulus means that we cannot discretize the channel using a regularly-spaced grid in r/θ coordinates without adaptation. We therefore transform the QG equations (34a)–(34b) into coordinates that follow the walls of the annulus,

$$\rho = R_w + \frac{(r - R_w)(R_c - R_w)}{(R_b - R_w)}, \quad \phi = \theta. \tag{35}$$

Here ρ is simply a rescaled radial coordinate that satisfies $\rho = R_w$ on $r = R_w$ and $\rho = R_c$ on $r = R_b$. Derivatives with respect to r and θ may be transformed to ρ, ϕ space by writing $q = q(\rho(r, \theta), \phi(\theta))$ and applying the chain rule,

$$\left.\frac{\partial q}{\partial r}\right|_\theta = \frac{(R_c - R_w)}{(R_b - R_w)} \left.\frac{\partial q}{\partial \rho}\right|_\phi, \tag{36a}$$

$$\left.\frac{\partial q}{\partial \theta}\right|_r = \left.\frac{\partial q}{\partial \phi}\right|_\rho + \frac{(\rho - R_w)}{(R_b - R_w)} \frac{\mathrm{d}W}{\mathrm{d}\phi} \left.\frac{\partial q}{\partial \rho}\right|_\phi. \tag{36b}$$

For example, the Jacobian operator in (34a) becomes

$$J(\psi, q) = \frac{1}{r(\rho, \phi)} \frac{(R_c - R_w)}{(R_b - R_w)} \left(\frac{\partial \psi}{\partial \rho} \frac{\partial q}{\partial \phi} - \frac{\partial \psi}{\partial \phi} \frac{\partial q}{\partial \rho} \right), \tag{37}$$

where $r(\rho, \phi)$ may be obtained by inverting (35). The Laplacian operator ∇^2 is considerably more complicated and includes a second-order cross-derivative in ρ and ϕ. We omit this expression for brevity.

5.2. Numerical integration

We discretize our dependent variables ψ, ζ and q on a grid of N_ρ by N_ϕ points with regular spacings Δ_ρ and Δ_ϕ respectively. We denote their positions as ρ_m for $m = 1, \ldots, N_\rho$ and ϕ_n for $n = 1, \ldots, N_\phi$, where $\rho_1 = R_w$ and $\rho_{N\rho} = R_c$. We denote variables stored at (ρ_m, ϕ_n) as, for example, $\psi_{m,n}(t)$, and for now we retain a continuous dependence on time for notational convenience. We approximate the Jacobian (37) using a second-order energy-conserving discretization [*Arakawa*, 1966], equivalent to rewriting (37) as a flux form and replacing derivatives with second-order central differences. We approximate the Laplacian operator in (34a) and (34b) using straightforward second-order central differencing in ρ, ϕ coordinates.

Our numerical scheme is simplified by the fact that the initial vorticity (10) is uniform. As the numerical viscosity acts only in the interior, (34a) states that the vorticity remains constant along the boundary, but decays exponentially with time scale κ^{-1}. This serves as a boundary condition for the relative vorticity, which may be written in ρ, ϕ coordinates as

$$\zeta\left(R_w, \phi, t\right) = \zeta\left(R_c, \phi, t\right) = \zeta_0(t), \quad \frac{\mathrm{d}\zeta_0}{\mathrm{d}t} = -\kappa\zeta_0. \tag{38}$$

with $\zeta_0(0) = -\Delta_f$. To simplify the presentation of our numerical scheme, we will assume for the moment that the streamfunction $\psi_0(t)$ on the outer wall is also a known function of time. We will explain how we evolve ψ_0 in §5.3.

We evolve the PV $q_{m,n}$ and streamfunction $\psi_{m,n}$ forward in time as follows. Given $q_{m,n}$ at all gridpoints at any time t, we first invert (34b) iteratively via successive over-relaxation to determine $\psi_{m,n}$ at all interior points, subject to

$$\psi_{1,n}(t) = 0, \quad \psi_{N_\rho,n}(t) = \psi_0(t), \quad n = 1, \ldots, N_\phi. \tag{39}$$

We then compute the right-hand side of (34a) at all interior grid points utilizing the vorticity boundary conditions

$$\zeta_{1,n}(t) = \zeta_{N_\rho,n}(t) = \zeta_0(t), \quad n = 1, \ldots, N_\phi, \tag{40}$$

to evaluate derivatives in the grid rows $m = 2$ and $m = N_\rho - 1$. This yields the time derivative of q at all interior grid points, which we use to step $q_{m,n}(t)$ forward in time using the third-order Adams–Bashforth scheme. We ensure that the fixed time step Δ_t satisfies the advective CFL condition throughout the integration.

For the purpose of comparison with our laboratory experiments, we track the position of the PV front that lies initially

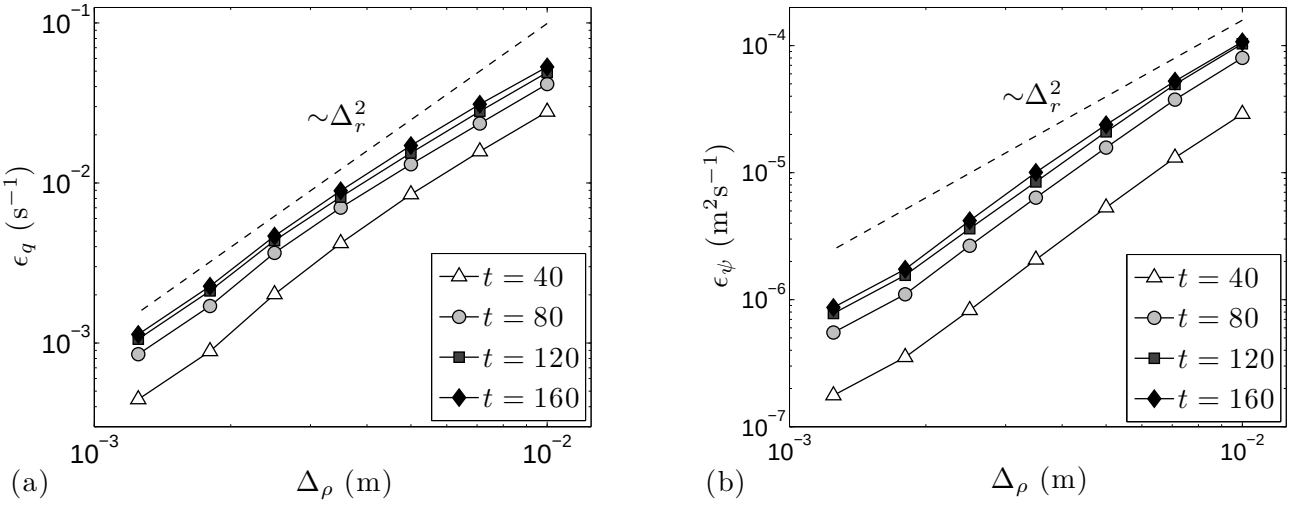

Figure 6. Verification of our numerical scheme, described in §5, for the test case $f = 1.5\,\mathrm{rad\,s^{-1}}$, $\Delta_f = 0.02\,\mathrm{rad\,s^{-1}}$. We plot the pointwise ℓ^2 error in (a) the PV and (b) the streamfunction between each solution and an "exact" solution obtained via Richardson extrapolation.

above the center of the slope. We accomplish this by advecting M passive tracer particles at (ρ_i, ϕ_i) for $i = 1, \ldots, M$ using the computed streamfunction $\psi_{m,n}(t)$. These particles are initially spread evenly around the shelf line, so

$$\rho_i(0) = R_w + \frac{(R_h - R_w)(R_c - R_w)}{(R_b(\phi_i(0)) - R_w)}, \quad \phi_i(0) = \frac{2\pi i}{M}. \quad (41)$$

Thereafter, at any time t the particle evolution is determined by

$$\frac{\mathrm{d}\rho_i}{\mathrm{d}t} = \frac{-1}{r(\rho_i, \phi_i)} \frac{(R_c - R_w)}{(R_b(\phi_i) - R_w)} \frac{\partial \psi}{\partial \phi}(\rho_i, \phi_i, t) \quad (42)$$

$$\frac{\mathrm{d}\phi_i}{\mathrm{d}t} = \frac{1}{r(\rho_i, \phi_i)} \frac{(R_c - R_w)}{(R_b(\phi_i) - R_w)} \frac{\partial \psi}{\partial \rho}(\rho_i, \phi_i, t). \quad (43)$$

At each time step, after inverting (34b) for $\psi_{m,n}$, we calculate $\partial\psi/\partial\rho$ and $\partial\psi/\partial\phi$ on each grid point via second-order central differencing. We then linearly interpolate these derivatives to compute the right-hand sides of (42) and (43). Finally, we integrate the particle positions forward in time using third-order Adams–Bashforth time-stepping.

5.3. Azimuthal transport

The above outline of our numerical algorithm assumes that the streamfunction $\psi_0(t)$ on the outer wall of the annulus is known. In fact, ψ_0 must evolve in such a way that either (14a) or (14b) is satisfied. We will focus on (14b) because it is more straightforward to evaluate numerically.

Following *Gresho* [1991a, b], we note that the solution ψ of (34b) may be decomposed as

$$\psi = \psi_P + \eta\,\psi_L, \quad (44)$$

where η is a constant to be determined and ψ_P and ψ_L solve Poisson's and Laplace's equations respectively,

$$\nabla^2\psi_P = \zeta, \qquad \nabla^2\psi_L = 0. \quad (45)$$

We choose $\psi_P = \psi_L = 0$ on $\rho = R_w$ to ensure that ψ vanishes on the inner wall, and without loss of generality set $\psi_P = 0$ and $\psi_L = \psi_{L0}$ on $\rho = R_c$, where ψ_{L0} may be any non-zero constant. Given ζ, this completely defines ψ_P and ψ_L, and so if we can determine η then ψ and ψ_0 follow trivially from (44).

We determine η by requiring that ψ_P and ψ_L satisfy (14b). We define Γ_P and Γ_L as the circulations due to ψ_P and ψ_L around the inner wall of the annulus,

$$\Gamma_j(t) = \int_0^{2\pi} \frac{R_w(R_c - R_w)}{(R_b - R_w)} \frac{\partial \psi_j}{\partial \rho}\mathrm{d}\phi, \quad (46)$$

for $j \in \{P, L\}$. It follows from (44) that

$$\Gamma_P + \eta\,\Gamma_L = \Gamma_w, \quad (47)$$

where Γ_w is determined at all times by (14b), and both Γ_P and Γ_L may be computed directly via (46). Thus (47) defines η, so the streamfunction on the outer wall is given by

$$\psi_0 = \psi_{L0}\frac{\Gamma_w - \Gamma_P}{\Gamma_L}. \quad (48)$$

In practice, we define ψ_{L0} and compute ψ_L and Γ_L once at the start of the numerical integration, and then at each time step we compute ψ_P, Γ_P and finally ψ.

The exception to the above procedure is at $t = 0$, when the initial circulation $\Gamma_w(0)$ is unknown. The initial transport $\psi_0(0)$ must then be chosen to ensure that (12a) and (12b) are equal. We compute $\psi_0(0)$ approximately using the asymptotic method described in §4.3, which defines $\psi_{m,n}(0)$ everywhere via (34b). We then calculate $\Gamma_w(0)$ directly from $\psi_{m,n}(0)$.

5.4. Convergence under grid refinement

We verify our numerical scheme by defining a test parameters $f = 1.5\,\mathrm{rad\,s^{-1}}$ and $\Delta_f = 0.02\,\mathrm{rad\,s^{-1}}$, whose behaviour is qualitatively similar to that shown in Figure 7. We compute solutions using these parameters over a range of grid spacings Δ_ρ increasing from 1.25 mm to 1 cm by factors of $\sqrt{2}$. In each case we integrate (34a) and (34b) up to $t = 180$, the typical length of our laboratory experiments. We choose $\Delta_\phi = \Delta_\rho/R_c$ so that Δ_ρ is the largest absolute distance between any two adjacent grid cells. We measure convergence towards an "exact" reference solution obtained via Richardson extrapolation from the two smallest grid spacings, which we denote as $(\psi_e)_{m,n}$ and $(q_e)_{m,n}$. We define the error between each of our computed solutions

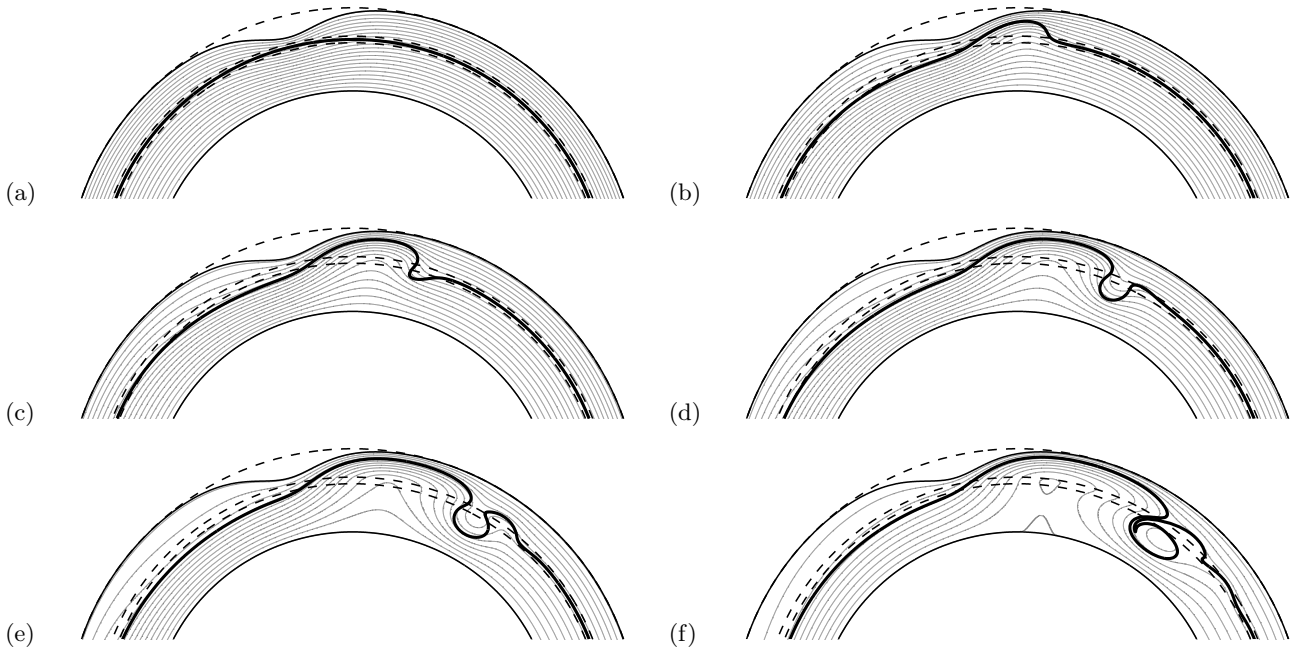

Figure 7. Evolution of the numerical solution of our QG model, described in §5, at (a) $t = 0\,\mathrm{s}$, (b) $t = 17\,\mathrm{s}$, (c) $t = 29\,\mathrm{s}$, (d) $t = 45\,\mathrm{s}$, (e) $t = 66\,\mathrm{s}$, and (f) $t = 104\,\mathrm{s}$. The numerical parameters have been chosen to match the reference experiment shown in Figure 3. In each snapshot we plot the the position of the passively-advected line of tracer (thick black line), and the instantaneous streamlines with a separation of $2\,\mathrm{cm}^2\,\mathrm{s}^{-1}$ (thin grey lines). The thin black lines show the positions of the inner and outer walls of the annulus, whilst the dashed lines highlight the extent of the slope and the width of the protrusion.

and the "exact" solution at any time t using the discrete ℓ^2 norm

$$\epsilon_q(t) = \sqrt{\sum_{m,n} (q_{m,n}(t) - (q_e)_{m,n}(t))^2}, \tag{49}$$

and similarly for $\epsilon_\psi(t)$.

In Figure 6 we plot ϵ_q and ϵ_ψ at four times over the course of our numerical integration. Both q and ψ exhibit convincing second-order convergence under grid refinement, owing to the smooth velocity field prescribed by our experimental conditions and the relatively short integration time. Our convergence study motivates the choice $\Delta_\rho = 2\,\mathrm{mm}$ for the purpose of comparison with our experimental results. The numerical viscosity has an unduly strong influence on the solution if the grid spacing is much larger than this ($\gtrsim 5\,\mathrm{mm}$) and PV is poorly conserved in filaments that cross the slope. It so happens that at $\Delta_\rho = 2\,\mathrm{mm}$, our prescribed numerical viscosity $A_n \sim 1 \times 10^{-6}\,\mathrm{m}^2\,\mathrm{s}^{-1}$ is comparable to the molecular viscosity of water in the experiments.

5.5. Comparison with experimental flows

Figure 7 characterizes the behaviour of solutions computed via the procedure outlined above. We use rotation parameters $f = 1.5\,\mathrm{rad\,s}^{-1}$ and $\Delta_f = 0.03\,\mathrm{rad\,s}^{-1}$, as in our reference experiment. The grid spacing of $\Delta_\rho = 2\,\mathrm{mm}$ results in a numerical grid of $N_\rho = 159$ by $N_\phi = 3347$ points. These parameters yield a numerical viscosity of $A_n = 1.5 \times 10^{-6}\,\mathrm{m}^2\,\mathrm{s}^{-1}$ and a bottom friction κ of approximately $6.1 \times 10^{-3}\,\mathrm{s}^{-1}$. The experimental dye is represented by $M = 3600$ tracer particles, visualized as a line in Figure 7.

The solution shown in Figure 7 is visibly similar to the evolution of the experimental dye line in Figure 3. In particular, the progression in Figure 7 of the solution from a long, smooth wave in panel (b) to a backward-breaking wave in panel (c) is strikingly similar to the behaviour of the experiment. However, the steepening of the wave, and in panel (d) the formation of the wave train, appear to happen more rapidly than they do in Figure 3. By eye, Figure 3(e) corresponds better to Figure 7(d) than Figure 7(e), despite being separated by 21 seconds. This may be due to imperfect conservation of PV on fluid columns crossing the experimental slope, or our bottom friction coefficient κ may simply be too small. In Figure 7 the two sides of the wave train in panel (e) do eventually curl up on themselves, as shown in panel (f), and as observed in our reference experiment. In §6 we will quantify this comparison over a range of Coriolis parameters and coastal current speeds.

A much larger volume of deep water is retained on the shelf in Figure 7(f) than in Figure 3, associated with the growth and persistence of the large-amplitude shelf wave. The streamlines reveal that the growth of this wave leads to constriction of the along-shelf flow. This drives water off the shelf and across the slope far upstream of the protrusion, resulting in acceleration of the incoming flow in the deeper portion of the channel. In panels (d)–(f) the wave envelope drives an exchange across the slope, drawing inflowing deep water onto the shelf at the protrusion and then exporting it further downstream. At $t = 104\,\mathrm{s}$ all inflowing deep water makes an excursion onto the shelf before continuing downstream. This is facilitated by patches of closed streamlines, corresponding to barotropic vortices/eddies in the flow that sustain the exchange of water across the slope.

6. Shelf wave breaking

The only consistent point of comparison between our numerical and experimental results is the formation of a breaking lee wave behind the bump in the outer wall of the channel. The evolution therafter varies widely across our parameter space in f and Δ_f. When the coastal current is weak and the background rotation strong, the breaking wave rapidly rolls up into eddies, which are beginning to form in Figures 3(f) and 7(f). A strong coastal current in the presence of weak background rotation will tend to inhibit wave breaking, and lead to the formation of a wave train resembling that in Figures 3(e) and 7(d). The wave breaking is

therefore the most natural point of comparison between our theory, numerical solutions, and experiments.

6.1. Breaking conditions

We obtain theoretical predictions of breaking wave properties using the nondispersive ($\gamma = 0$) form of the nonlinear shelf wave equation (28). The dispersive form ($\gamma = 1$) is formally more accurate but inhibits shock formation, which describes wave breaking in our theoretical framework. For each parameter combination (f, Δ_f) we solve (28) on an azimuthal grid of $N = 7200$ points using the method described in §4.5. We define the solution to have formed a shock, and thus the wave to have broken, when the gradient of the interface $r = R(\theta, t)$ satisfies

$$\max_{\theta\in[0,2\pi)} \left| \frac{1}{R}\frac{\partial R}{\partial \theta} \right| > S_{\max}. \tag{50}$$

The gradient threshold $S_{\max}$ should be maximized to ensure that interface has come as close as possible to a discontinuity before (50) is satisfied. We use $S_{\max} = 20$ because the pseudo-spectral solution cannot reach much larger gradients on a grid of size $N = 7200$ without becoming subject to Gibbs' phenomenon.

In our numerical solutions we track the positions $(\rho_i(t), \phi_i(t))$ for $i = 1, \ldots, M$ of tracer particles that lie initially over the center of the slope. We deem the waveform comprised of these particles to have broken when any two adjacent particles occupy the same azimuthal position, *i.e.*

$$\phi_i(t) > \phi_{i+1}(t), \quad \text{for any} \quad i = 1, \ldots, M. \tag{51}$$

The addition $i + 1$ is taken modulo M because particle positions wrap around the annulus.

We identify wave breaking in our experimental results by processing the images of the tank to extract the positions of the dye line in each frame. Our focus on the initial development and breaking of the wave permits the use of a simplified algorithm, because the dye-line may be described as a single-valued function of azimuthal position. Each image is first filtered to remove shades dissimilar to that of the dye line. Then at each azimuthal position θ_p for $p = 1, \ldots, P$, we search radially to locate the midpoint of the dye line, which we denote as R_p. We thereby construct a series of points along the dye line in each frame, $(\theta_p, R_p(t))$, similar to our description of the interface $R(\theta, t)$ in our nonlinear wave theory. We omit azimuthal positions θ_p obscured by the clamps visible in Figure 2, and successive frames are compared to remove erroneous measurements due to the dye dispenser. We deem the wave to have broken by applying a condition analogous to (50), but using the mean gradient over a small range of θ to eliminate noise that arises from the image filtering. In practice the choice of $S_{\max}$ and the filtering must be adjusted to each experiment due variations in the colour of the dye line and the hues of the images.

6.2. Onset of wave breaking

The time at which the wave first breaks serves as a direct quantitative comparison of our theoretical, numerical and experimental results. It is also an indication of how effectively PV is conserved as fluid crosses the shelf line, as waves of the same length will tend to steepen more quickly if they entrain a larger relative vorticity. In our theory, numerical solutions, and experiments, we define T_B as the smallest t for which the corresponding wave breaking condition is satisfied. In Figures 8(a), 9(a) and 10(a) we plot T_B over our experimental ranges of f and Δ_f, as calculated from our nonlinear wave theory, our numerical solutions, and our experiments respectively.

The variation of T_B with f and Δ_f is qualitatively similar in our nonlinear wave theory and QG numerical solutions: a swift coastal current or strong rotation lead to the wave breaking much more rapidly than a slow current or weak rotation. However, solutions of the nonlinear wave equation break more than twice as quickly. This reflects the fact that the continuous slope used in our numerical solutions results in a finite-width PV front, whereas the theory describes a discontinuous front. The resulting wave envelops a smaller net relative vorticity, particularly during its initial formation, and therefore steepens less rapidly. The long-wave approximation used to derive (28) also fails when the gradient of the interface $R(\theta, t)$ becomes $\mathcal{O}(1)$, and this may exaggerate the rate at which the wave steepens and breaks.

Figure 10(a) shows that T_B is again qualitatively similar in our experiments and numerical solutions. In Figure 11(a) we plot the relative error in the numerically-computed breaking times, $\Delta T_B = T_{B\,\text{numerical}}/T_{B\,\text{experiment}} - 1$. The QG model tends to under-predict T_B relative to the laboratory experiments, typically by a factor of $\sim 2/3$. This indicates that PV is imperfectly conserved in our experimental channel, particularly given the similarities in the wavelength at breaking (see §6.3). This may be due to stronger bottom friction acting over the experimental shelf and slope, as discussed in §3.1.

6.3. Breaking wavelength

We now turn our attention to the length of the lee wave at breaking. Apart from being a useful way to quantify the closeness of our QG solutions and laboratory experiments, the breaking wavelength determines the scale of the eddies that form behind the protrusion. We define L_B as the distance along the shelfline between the azmiuthal position (θ, ϕ_i or θ_p) at which the wave has broken (θ_B), and the smallest subsequent $\theta > \theta_B$ at which the wave envelope lies below the shelf line $r = R_h$. In Figures 8(b), 9(b) and 10(b) we compare L_B between our nonlinear wave theory, numerical solutions, and experiments. Here have converted L_B to distances in cm along the shelf line.

As with T_B in §6.2, we find that L_B has a qualitatively similar dependence on f and Δ_f in our theory and numerical solutions. A swift coastal current or weak background rotation yields a long wave at breaking, because water is drawn further onto the shelf by the mean flow before the relative vorticity it acquires can steepen and break the wave. Waves evolving under the nonlinear wave equation break at approximately half the length of the waves in our numerical solutions, consistent with their shorter breaking time. The nonlinear wave theory predicts an unusually large L_B for $f = 3\,\text{rad}\,\text{s}^{-1}$ and $\Delta_f = 0.01\,\text{rad}\,\text{s}^{-1}$. In this corner of parameter space the wave speed given by (28) exceeds the mean flow speed at the protrusion, for sufficiently small perturbations of the interface R about the shelf line $r = R_h$. This allows the wave envelope to propagate further upstream, resulting in a larger wavelength at breaking.

The breaking wavelength shows good qualitative and quantitative agreement between our numerical solutions and laboratory experiments. In Figure 11(b) shows that the relative error in the numerically-computed breaking lengths, $\Delta L_B = L_{B\,\text{numerical}}/L_{B\,\text{experiment}} - 1$, is consistently below 20%. This is surprising because the experimental waves take longer to break, and so may be expected to be longer than numerically-computed waves advected by the same mean flow. This may be due to a canceling effect with the smaller amplitudes of the experimental waves (see 6.4), which results in much shorter wavelengths due to the small aspect of the wave envelope.

6.4. Amplitude at breaking

Lastly, we analyse the amplitudes of the waves at the point of breaking. This is directly relevant to the cross-slope exchange of ocean waters, as it serves as a measure of the volume transported onto the shelf due to advection past the protrusion. We define the breaking amplitude A_B as the largest radial extent of the wave envelope, measured from $r = R_h$, between θ_B and $\theta_B + L_B$. We plot A_B for our theory, numerical solutions and experiments in Figures 8(c), 9(c) and 10(c) respectively.

In this case there is a contrast between the amplitudes predicted by the nonlinear shelf wave theory and the numerical solutions. In Figure 8(c), A_B is largest for swift coastal currents (large Δ_f) and weak background rotation (small f), and vice versa. Figure 9(c) exhibits a similar pattern when the coastal current is weak, but for sufficiently large Δ_f we find that A_B instead increases with f. This reflects the action of two competing effects on the amplitude of the wave envelope: stronger relative vorticity within the wave envelope drives a stronger flow onto the shelf, but also induces breaking more rapidly (see §6.2). The former is poorly represented in our long-wave theory, which implicitly assumes a small ratio of cross-slope to along-slope transport. We have re-calculated Figue 8(c) using the full dispersive wave equation (28), with a much smaller gradient $\S_{\max}$ in (50), but this still fails to capture the pattern shown in Figure 9(c).

The patterns of A_B in Figure 10(c) is qualitatively similar to Figure 9(c), albeit somewhat distorted because A_B is particularly sensitive to artifacts in the filtered experimental images. In Figure 11(c) we plot the relative error in the numerically-computed amplitudes at breaking, $\Delta A_B = A_{B\,\text{numerical}}/A_{B\,\text{experiment}} - 1$. The wave amplitude is typically around 1–2 cm larger in our numerical solutions than in our experiments. We attribute this to our assumption of horizontally non-divergent flow under the QG approximation, which neglects depth changes in the mass conservation equation. Our numerical solutions therefore overestimate the volume of fluid drawn onto the shelf in the lee of the protrusion in the outer wall.

7. Summary and discussion

The large-scale flow of coastal currents is dominated by the interaction of the current with the strong topographic PV gradient at the continental shelf break, which results in complex behaviour even in a strongly barotropic fluid. This has motivated previous experimental studies ranging from generation of isolated topographic Rossby waves [*Ibbetson and Phillips*, 1967; *Caldwell et al.*, 1972; *Cohen et al.*, 2010] to turbulent coastal currents [*Cenedese et al.*, 2005; *Sutherland and Cenedese*, 2009]. This chapter has focused on the flow of a retrograde coastal current past a headland that protrudes out onto the continental shelf. Examples of such a configuration include the flow of the Agulhas current through the Mozambique Channel [*Bryden et al.*, 2005; *Beal et al.*, 2006, 2011], and Gulf Stream's approach to Cape Hatteras [*Stommel*, 1972; *Johns and Watts*, 1986; *Pickart*, 1995].

In §2 we introduced our laboratory experiments, whose set-up is sketched in Figure 1 and illustrated in Figure 2. We constructed an annular channel in a rotating tank with a narrow slope leading to a raised shelf around the outer rim. The shelf was constricted over an azimuthal length $\sim \Theta_b$ by a protrusion in the outer wall, representing a continental headland. We generated a retrograde azimuthal mean flow, representing a coastal current, by changing the rate of the tank's rotation. This resulted in the formation of a large-amplitude Rossby shelf wave in the lee of the protrusion, which we visualised using a dye line that was positioned initially along the centre of the PV front. Figure 3 characterises the evolution of the flow, which develops a long, large-amplitude shelf wave that breaks and overturns. Thereafter the wave may unravel and form a wave train, as shown in Figure 3(e), or may instead roll up into eddies.

To interpret the behaviour of our experimental shelf waves, we introduced in §3 a QG shallow water model. The model assumes non-divergent, geostrophically-balance barotropic flow beneath a rigid lid and with negligible variations in depth. We applied no-flux boundary conditions for the channel walls, and prescribed initial conditions that conserve the absolute vorticity of each fluid column, and the total kinetic energy, during the initial change in the tank's rate of rotation. Some discrepancy is to be expected between this model and our experiments, in which the surface height may vary across the channel and the shelf occupies a quarter of the water depth. However, QG theory has been shown to describe rapidly-rotating laboratory flows far outside the formal range of validity [*Williams et al.*, 2010], and retains the vortical dynamics required to capture the evolution of shelf waves [*Johnson and Clarke*, 2001].

In §4 we derived a nonlinear wave theory to provide an intuitive description of the shelf wave evolution. Our theory follows that of *Haynes et al.* [1993] and *Clarke and Johnson* [1999] for a straight channel, approximating the slope as a discontinuity in depth and posing an asymptotic expansion in a small parameter that measures the ratio of the wave amplitude to the wavelength. The theory does not require the wave amplitude to be small, however: making this additional assumption yields a Korteweg–de Vries-like equation [*Johnson and Clarke*, 1999]. Our nonlinear wave equation (28) improves upon the derivations of *Stewart* [2010] and *Stewart et al.* [2011] via the addition of an evolution equation (30) for the streamfunction on the outer wall. Figure 4 shows that the evolution of the first-order nonlinear wave equation initially resembles our experimentally-generated waves, but dispersion prevents these solutions from capturing the wave breaking. By contrast, solutions of the non-dispersive zeroth-order wave equation will always break, but thereafter form a persistent shock that does not resemble the experimental flows.

To resolve the disparity between our experiments and our long-wave theory, in §5 we developed a numerical scheme that solves the QG model equations in a wall-following coordinate system. We advect an array of tracer particles that delineates the wave envelope, mimicking the dye line in our laboratory experiments. Figure 7 shows that the numerical shelf wave is qualitatively similar to our laboratory experiments, but the evolution occurs more rapidly. This may be due to imperfect conservation of PV or stronger bottom friction in the rotating tank. The numerical solution shows that regions of closed streamlines appear as the shelf wave curls up, forming eddies that transport water across the slope.

In §6 we compared shelf waves formed in our long-wave theory, numerical solutions, and laboratory experiments. The clearest point of comparison between the three is initial breaking of the wave; the evolution therafter varies widely, impeding quantitative comparison. In our long-wave theory a stronger coastal current (Δ_f) results in a larger PV flux across the slope, leading to longer shelf waves with larger amplitudes that break more rapidly. Stronger rotation f produces a larger relative vorticity in the wave envelope, resulting in shelf waves that break more rapidly at smaller wavelengths and amplitudes. Our numerical and experimental results exhibit similar patterns of breaking time (T_B) and wavelength at breaking (L_B), but the amplitude at breaking (A_B) may increase or decrease with f, depending on the size of Δ_f. We attribute this to competing tendencies for the wave to transport more water across the slope, but also to break more rapidly, when the relative vorticity in the wave envelope is larger. Figure 11 compares the properties

of breaking in our numerical solutions and laboratory experiments. Whilst L_B is consistently within around 20% error, our QG model under-predict T_B and over-predict A_B, in each case by a factor of 1/3 on average. This is again consistent with imperfect conservation of PV or stronger bottom friction in the rotating tank.

The large amplitude of our coastal shelf waves distinguishes our experiments from previous studies of topographic Rossby wave generation, and the development of a nonlinear wave theory aids in interpreting our results (see §4). Previous investigations of Rossby waves over continental slopes, such as those of *Caldwell et al.* [1972], *Caldwell and Eide* [1976] and *Cohen et al.* [2010], have shown very good agreement with the corresponding theoretical dispersion relations. *Pierini et al.* [2002] found that numerical solutions of the barotropic shallow water equations closely reproduced Rossby normal modes on an experimental slope between two walls. Our QG numerical solutions accurately describe the evolution of our experiments, as shown in §6. This indicates that flow in the rotating tank adheres closely to columnar motion, despite the formal requirements for the shallow water-QG approximation being poorly satisfied [see *Williams et al.*, 2010].

Solutions of the nonlinear shelf wave equation in §4 differ substantially from our experimental results. Our nonlinear wave theory cannot capture the overturning of the wave and the resulting break-up into eddies, due to the assumption of a single-valued interface $r = R(\theta, t)$. The theory should to describe the flow accurately as long as the azimuthal gradients remain $\mathcal{O}(\mu^{1/2})$, which is certainly the case during the initial generation of the wave. The dispersive terms in (28) may be expected to inhibit wave steepening, and thereby maintain a small amplitude-to-wavelength ratio, as in Figure 4. It is therefore unclear why the numerical and experimental shelf waves develop gradients that are $\mathcal{O}(1)$ within 10–50 s. The formation of a wave train in Figures 3 and 7 indicate that some dispersion takes place, but that it is not sufficient to prevent breaking. This phenomenon is the subject of ongoing research.

Previous laboratory investigations of coastal currents have focused on buoyant gravity currents [*Whitehead and Chapman*, 1986; *Cenedese and Linden*, 2002; *Folkard and Davies*, 2001; *Wolfe and Cenedese*, 2006; *Sutherland and Cenedese*, 2009] or turbulent jets [*Cenedese et al.*, 2005]. Our experiments employ a barotropic coastal current generated via a rapid change in the tank's rotation rate. Such a configuration has received little attention in previous laboratory studies, though *Pierini et al.* [2002] generated a barotropic shoreward mean flow using a wide, slow-moving plunger. Our use of dye to visualize our experimental results implicitly describes the evolution of the coastal current as a wave. This may be insufficient for more realistic bathymetry like the coastal trough of *Sutherland and Cenedese* [2009], though their trough-crossing current resembles a trapped topographic Rossby wave [*Kaoullas and Johnson*, 2012]. The wave-like description of the current breaks down when eddies form, as in the experiments of *Folkard and Davies* [2001] and *Wolfe and Cenedese* [2006], and in the long-term evolution of our experimental and numerical coastal currents.

Our results show that retrograde coastal current flow past a continental headland shifts the PV front shoreward from the continental slope. The resulting large-amplitude lee wave breaks, and subsequently tends to form eddies that exchange water between the coastal waters and the deep ocean. However, if the velocity of the current is sufficiently large then the wave and any eddies are simply swept away downstream. Our parameter sweep in §6 yields insight into the eddies formed by the wave breaking, and the resulting exchange of water across the shelf break. For the purpose of comparison with the real ocean, Δ_f measures the velocity of the coastal current, and f measures the PV jump between the continental shelf and the open ocean. The lee wave is longest, resulting in the largest eddies, when the coastal current is strong and the PV jump is small. We measure the penetration of open ocean water onto the experimental shelf using the amplitude of the lee wave at breaking. In general, water is transported further onto the shelf when the coastal current is strong and the PV jump is large, but the complete dependence on f and Δ_f is somewhat more complicated (see §6.4).

There is a developed body of theory that describes the evolution of coastal currents in terms of shelf waves [*e.g. Mysak*, 1980b; *Johnson and Clarke*, 2001]. Predictive models of coastal shelves require adaptation for the sharply-varying bathymetry, and must employ very high resolution to capture the shelf processes [*e.g. Haidvogel et al.*, 2008]. As a result, there remains scope for laboratory experiments to inform oceanographic research on the subject of continental shelf dynamics, and to evaluate numerical ocean models. It would be particularly valuable to perform further experiments with strongly nonlinear flows, such as the evolution of turbulent boundary currents [*Sutherland and Cenedese*, 2009], generation of geostrophic eddies over the continental slope [*Pennel et al.*, 2012], or the nonlinear shelf waves considered here.

Acknowledgments. This research was supported by an EPSRC DTA award to A.L.S. and by the Summer Study Program in Geophysical Fluid Dynamics at Woods Hole Oceanographic Institution, funded by NSF grant OCE-0824636 and ONR grant N00014-09-10844. P.J.D.'s research is supported by an EPSRC Advanced Research Fellowship, grant number EP/E054625/1. The authors thank Jack Whitehead for granting them use of the GFD laboratory at Woods Hole Oceanographic Institution, and thank Anders Jensen for indispensible assistance and advice in constructing and conducting the experiments described herein.

References

Allen, J. S., Models of wind-driven currents on the continental shelf, *Ann. Rev. Fluid Mech.*, *12*, 389–433, 1980.

Arakawa, A., Computational design for long-term numerical integration of the equations of fluid motion: Two-dimensional incompressible flow. Part I, *J. Comp. Phys.*, *1*, 119–143, 1966.

Beal, L. M., T. K. Chereskin, Y. D. Lenn, and S. Elipot, The sources and mixing characteristics of the Agulhas Current, *J. Phys. Oceanogr.*, *36*, 2060–2074, 2006.

Beal, L. M., W. P. M. De Ruijter, A. Biastoch, and R. Zahn, On the role of the Agulhas system in ocean circulation and climate, *Nature*, *472*, 429–436, 2011.

Boyd, J. P., *Chebyshev and Fourier spectral methods*, Dover, 2001.

Brink, K. H., Coastal-trapped waves and wind-driven currents over the continental shelf, *Ann. Rev. Fluid Mech.*, *23*, 389–412, 1991.

Bryden, H. L., L. M. Beal, and L. M. Duncan, Structure and transport of the Agulhas Current and its temporal variability, *J. Oceanogr.*, *61*, 479–492, 2005.

Buchwald, V., and W. Melville, Resonance of shelf waves near islands, in *Waves on Water of Variable Depth*, pp. 202–205, Springer, 1977.

Buchwald, V. T., and J. K. Adams, The propagation of continental shelf waves, *Proc. Roy. Soc. A*, *305*, 235–250, 1968.

Caldwell, D. R., and S. A. Eide, Experiments on the resonance of long-period waves near islands, *Proc. Roy. Soc. A*, *348*, 359–378, 1976.

Caldwell, D. R., D. L. Cutchin, and M. S. Longuet-Higgins, Some model experiments on continental shelf waves, *J. Mar. Res.*, *30*, 39–55, 1972.

Carnevale, G. F., S. G. Llewellyn Smith, F. Crisciani, R. Purini, and R. Serravall, Bifurcation of a coastal current at an escarpment, *J. Phys. Oceanogr.*, *29*, 969–985, 1999.

Cenedese, A., C. Vigarie, and E. V. Di Modrone, Effects of a topographic gradient on coastal current dynamics, *J. Geophys. Res.*, *110*, C09,009, 2005.

Cenedese, C., and P. F. Linden, Stability of a buoyancy-driven coastal current at the shelf break, *J. Fluid Mech.*, *452*, 97–121, 2002.

Clarke, S. R., and E. R. Johnson, Finite-amplitude topographic Rossby waves in a channel, *Phys. Fluids*, *11*, 107–120, 1999.

Cohen, Y., N. Paldor, and J. Sommeria, Laboratory experiments and a non-harmonic theory for topographic rossby waves over a linearly sloping bottom on the f-plane, *J. Fluid Mech.*, *645*, 479–496, 2010.

Cohen, Y., N. Paldor, and J. Sommeria, Application of laboratory experiments to assess the error introduced by the imposition of "wall" boundary conditions in shelf models, *Ocean Modell.*, *41*, 35–41, 2012.

Colin de Verdiere, A., Mean flow generation by topographic Rossby waves, *J. Fluid Mech*, *94*, 39–64, 1979.

Folkard, A. M., and P. A. Davies, Laboratory studies of the effects of interrupted, sloping topography on intermediate depth boundary currents in linearly stratified fluids, *Dynam. Atmos. Ocean.*, *33*, 239–261, 2001.

Gill, A. E., and E. H. Schumann, Topographically induced changes in the structure of an inertial coastal jet: Application to the Agulhas Current, *J. Phys. Oceanogr.*, *9*, 975–991, 1979.

Gordon, A. L., Indian-Atlantic transfer of thermocline water at the Agulhas Retroflection, *Science*, *227*, 1030–1033, 1985.

Gordon, A. L., Interocean exchange of thermocline water, *J. geophys. Res*, *91*, 5037–5046, 1986.

Gresho, P. M., Incompressible fluid dynamics: Some fundamental formulation issues, *Ann. Rev. Fluid Mech.*, *23*, 413–453, 1991a.

Gresho, P. M., Some current CFD issues relevant to the incompressible Navier-Stokes equations, *Comp. Meth. Appl. Mech. Eng.*, *87*, 201–252, 1991b.

Haidvogel, D. B., et al., Ocean forecasting in terrain-following coordinates: Formulation and skill assessment of the Regional Ocean Modeling System, *J. Comp. Phys.*, *227*, 3595–3624, 2008.

Haynes, P. H., E. R. Johnson, and R. G. Hurst, A simple model of Rossby-wave hydraulic behaviour, *J. Fluid Mech.*, *253*, 359–384, 1993.

Hou, T. Y., and R. Li, Computing nearly singular solutions using pseudo-spectral methods, *J. Comput. Phys.*, *226*, 379–397, 2007.

Ibbetson, A., and N. Phillips, Some laboratory experiments on rossby waves in a rotating annulus, *Tellus*, *19*, 81–87, 1967.

Johns, W. E., and D. R. Watts, Time scales and structure of topographic Rossby waves and meanders in the deep Gulf Stream, *J. Mar. Res.*, *44*, 267–290, 1986.

Johnson, E., Topographic waves in elliptical basins, *Geophy. Astro. Fluid*, *37*, 279–295, 1987.

Johnson, E. R., Topographic waves and the evolution of coastal currents, *J. Fluid Mech.*, *160*, 499–509, 1985.

Johnson, E. R., and S. R. Clarke, Dispersive effects in Rossby-wave hydraulics, *J. Fluid Mech.*, *401*, 27–54, 1999.

Johnson, E. R., and S. R. Clarke, Rossby Wave Hydraulics, *Ann. Rev. Fluid Mech.*, *33*, 207–230, 2001.

Johnson, E. R., and M. K. Davey, Free-surface adjustment and topographic waves in coastal currents, *J. Fluid Mech.*, *219*, 273–289, 1990.

Johnson, E. R., and G. Kaoullas, Bay-trapped low-frequency oscillations in lakes, *Geophys. Astro. Fluid*, *105*, 48–60, 2011.

Johnson, E. R., J. T. Rodney, and G. Kaoullas, Trapped modes in coastal waveguides, *Wave Motion*, *49*, 212–216, 2012.

Kaoullas, G., and E. R. Johnson, Geographically localised shelf waves on curved coasts, *Cont. Shelf Res.*, *30*, 1753–1760, 2010.

Kaoullas, G., and E. R. Johnson, Isobath variation and trapping of continental shelf waves, *J. Fluid Mech.*, *700*, 283–303, 2012.

Longuet-Higgins, M. S., On the trapping of waves along a discontinuity of depth in a rotating ocean, *J. Fluid Mech.*, *31*, 417–434, 1968.

Martinson, D. G., S. E. Stammerjohn, R. A. Iannuzzi, R. C. Smith, and M. Vernet, Western Antarctic Peninsula physical oceanography and spatio–temporal variability, *Deep Sea Res. Pt. II*, *55*, 1964–1987, 2008.

McWilliams, J. C., A note on a consistent quasigeostrophic model in a multiply connected domain, *Dynam. Atmos. Oceans*, *1*, 427–441, 1977.

Minobe, S., A. Kuwano-Yoshida, N. Komori, S. P. Xie, and R. J. Small, Influence of the gulf stream on the troposphere, *Nature*, *452*, 206–209, 2008.

Mysak, L. A., Topographically trapped waves, *Ann. Rev. Fluid Mech.*, *12*, 45–76, 1980a.

Mysak, L. A., Recent advances in shelf wave dynamics, *Rev. Geophys.*, *18*, 211–241, 1980b.

Mysak, L. A., P. H. Leblond, and W. J. Emery, Trench waves, *J. Phys. Oceanogr.*, *9*, 1001–1013, 1979.

Nittrouer, C. A., and L. D. Wright, Transport of particles across continental shelves, *Rev. Geophys.*, *32*, 85–113, 1994.

Pedlosky, J., *Geophysical Fluid Dynamics*, Springer, 1987.

Pennel, R., A. Stegner, and K. Béranger, Shelf impact on buoyant coastal current instabilities, *J. Phys. Oceanogr.*, *42*, 39–61, 2012.

Pickart, R. S., Gulf Stream-generated topographic Rossby waves, *J. Phys. Oceanogr.*, *25*, 574–586, 1995.

Pierini, S., A. M. Fincham, D. Renouard, M. R. D'Ambrosio, and H. Didelle, Laboratory modeling of topographic Rossby normal modes, *Dyam. Atmos. Ocean.*, *35*, 205–225, 2002.

Prézelin, B. B., E. E. Hofmann, M. Moline, and J. M. Klinck, Physical forcing of phytoplankton community structure and primary production in continental shelf waters of the Western Antarctic Peninsula, *J. Mar. Res.*, *62*, 419–460, 2004.

Rodney, J. T., and E. R. Johnson, Localisation of coastal trapped waves by longshore variations in bottom topography, *Cont. Shelf Res.*, pp. 130–137, 2012.

Sommeria, J., S. D. Meyers, and H. L. Swinney, Experiments on vortices and Rossby waves in eastward and westward jets, *Nonlinear Topics in Ocean Physics*, *109*, 227–269, 1991.

Stewart, A. L., Nonlinear shelf waves in a rotating annulus, *Technical Report of the 2009 Geophysical Fluid Dynamics Program at Woods Hole Oceanographic Institution*, pp. 373–402, 2010.

Stewart, A. L., P. J. Dellar, and E. R. Johnson, Numerical simulation of wave propagation along a discontinuity in depth in a rotating annulus, *Comput. Fluids*, *46*, 442–447, 2011.

Stommel, H., *The Gulf Stream: a physical and dynamical description*, Univ of California Press, 1972.

Sutherland, D. A., and C. Cenedese, Laboratory experiments on the interaction of a buoyant coastal current with a canyon: Application to the East Greenland Current, *J. Phys. Oceanogr.*, *39*, 1258–1271, 2009.

Thompson, A. F., and K. J. Heywood, Frontal structure and transport in the northwestern Weddell Sea, *Deep-Sea Res. I*, *55*, 1229–1251, 2008.

Vallis, G. K., *Atmospheric and oceanic fluid dynamics: fundamentals and large-scale circulation*, Cambridge University Press, 2006.

Whitehead, J., and D. C. Chapman, Laboratory observations of a gravity current on a sloping bottom: the generation of shelf waves, *J. Fluid Mech.*, *172*, 373–99, 1986.

Williams, P. D., P. L. Read, T. W. N. Haine, et al., Testing the limits of quasi-geostrophic theory: application to observed laboratory flows outside the quasi-geostrophic regime, *J. Fluid Mech.*, *649*, 187, 2010.

Wolfe, C. L., and C. Cenedese, Laboratory experiments on eddy generation by a buoyant coastal current flowing over variable bathymetry, *J. Phys. Oceanogr.*, *36*, 395–411, 2006.

Paul J. Dellar, Oxford Centre for Industrial and Applied Mathematics, University of Oxford, 24–29 St Giles', Oxford, OX1 3LB, UK. (dellar@maths.ox.ac.uk)

A. L. Stewart, Environmental Sciences and Engineering, Linde + Robinson Laboratory, California Institute of Technology, Pasadena, CA 91125, USA. (stewart@gps.caltech.edu)

Edward R. Johnson, Department of Mathematics, University College London, Gower Street, London, WC1E 6BT, UK. (e.johnson@ucl.ac.uk)

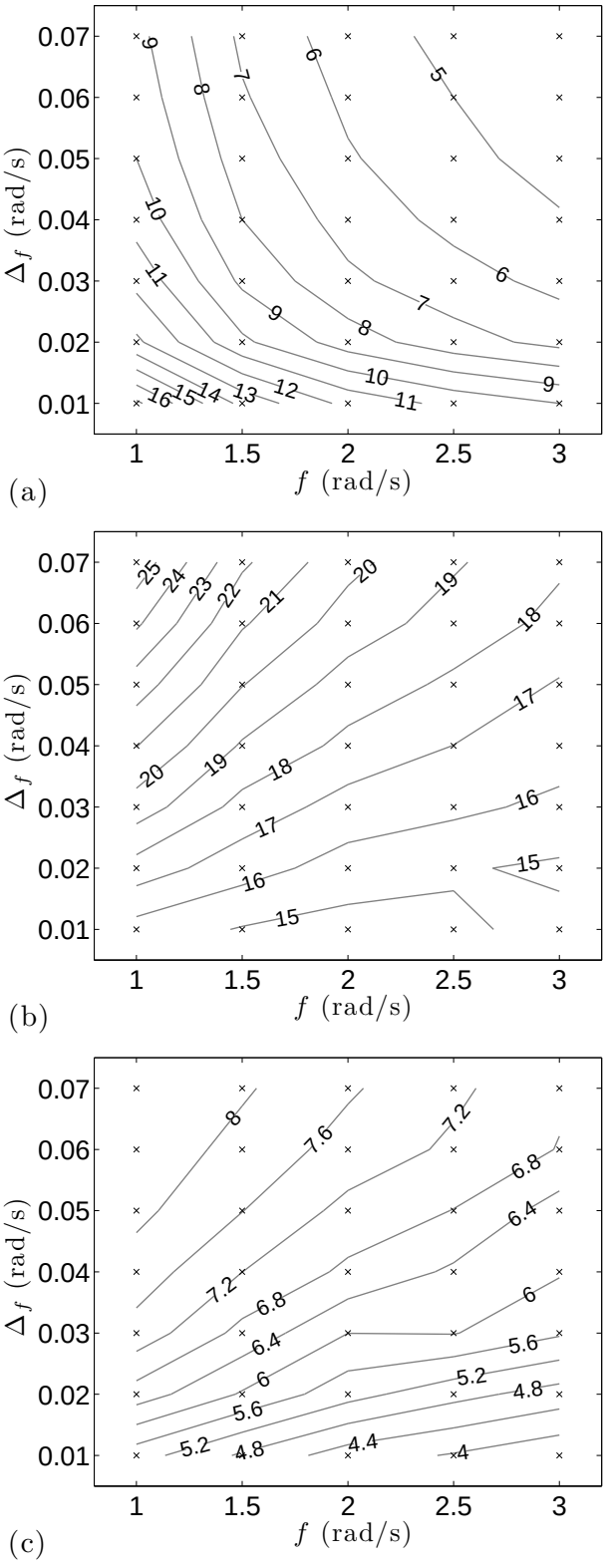

Figure 8. Contour plots of (a) the time of wave breaking in seconds, (b) the breaking wave length in cm, and (c) the breaking wave amplitude in cm, calculated using the nondispersive ($\gamma = 0$) wave equation (28). The contours have been interpolated linearly between data points, which are indicated by crosses.

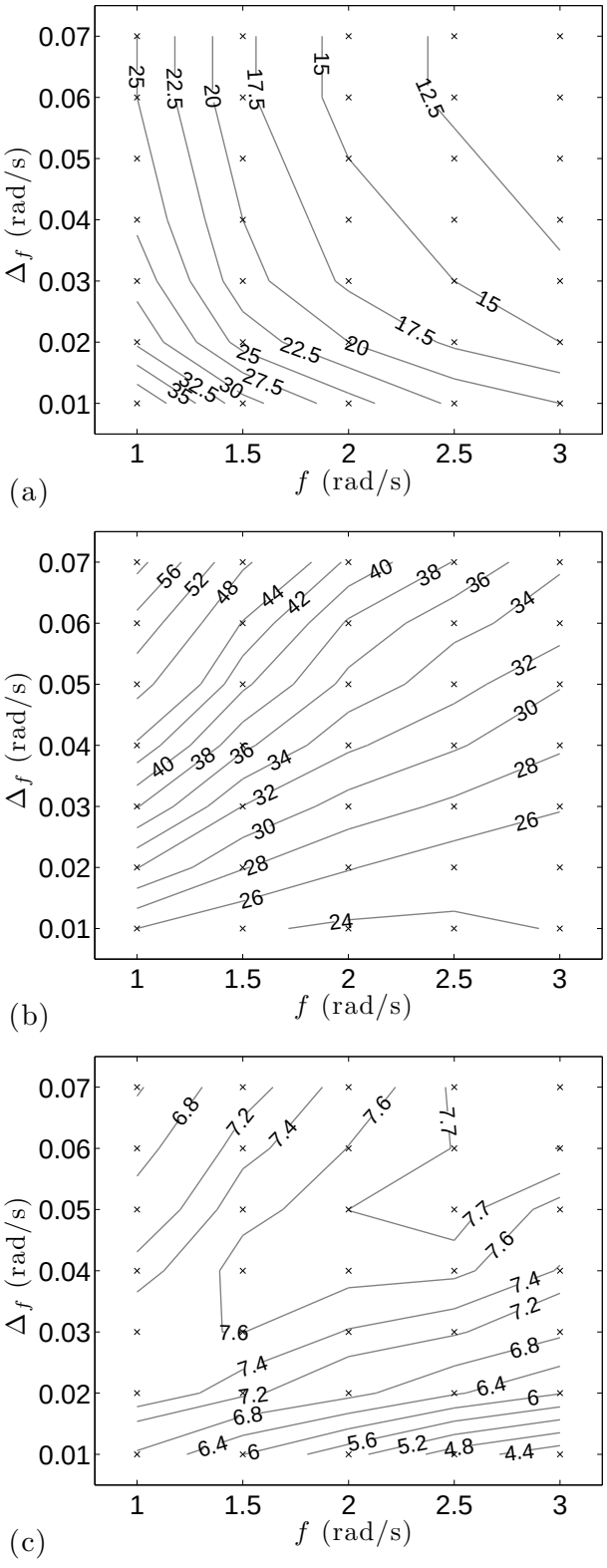

Figure 9. Contour plots of (a) the time of wave breaking in seconds, (b) the breaking wave length in cm, and (c) the breaking wave amplitude in cm computed in numerical solutions of the QG model equations (34a)–(34b). The contours have been interpolated linearly between data points, which are indicated by crosses.

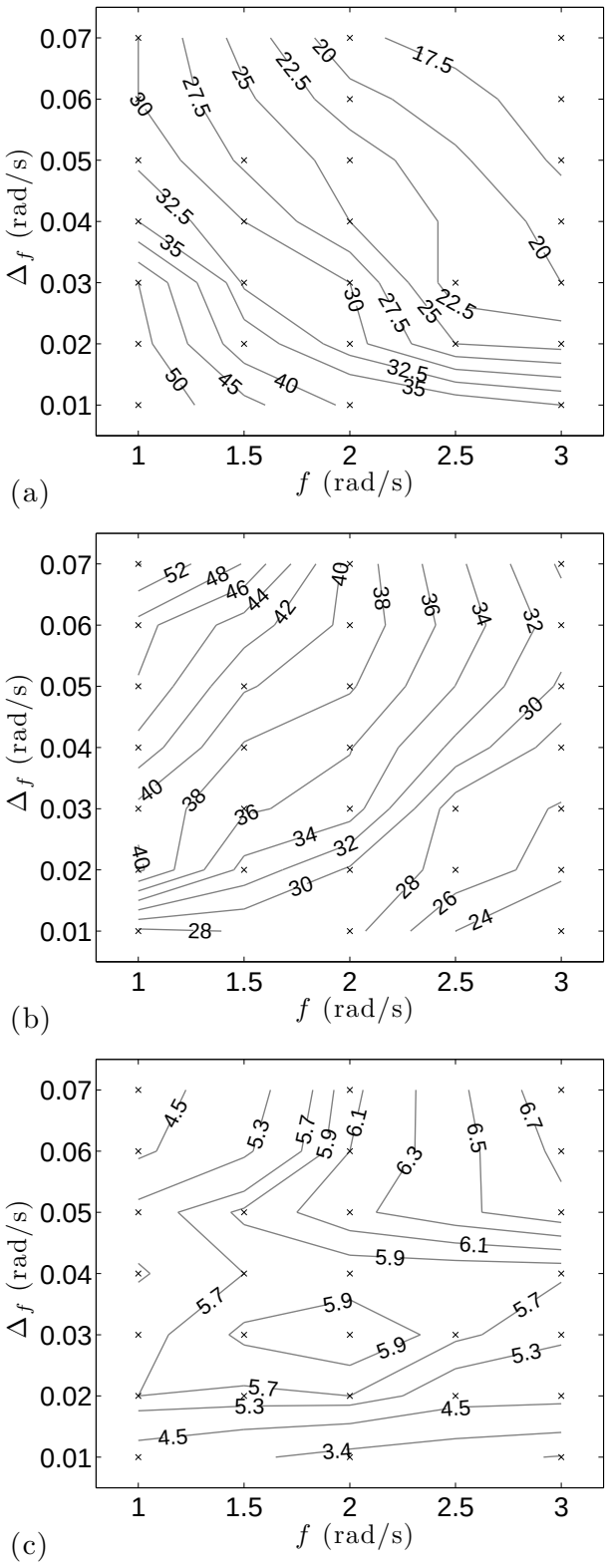

Figure 10. Contour plots of (a) the time of wave breaking in seconds, (b) the breaking wave length in cm, and (c) the breaking wave amplitude in cm, extracted from our experimental results. The contours have been interpolated linearly between data points, which are indicated by crosses.

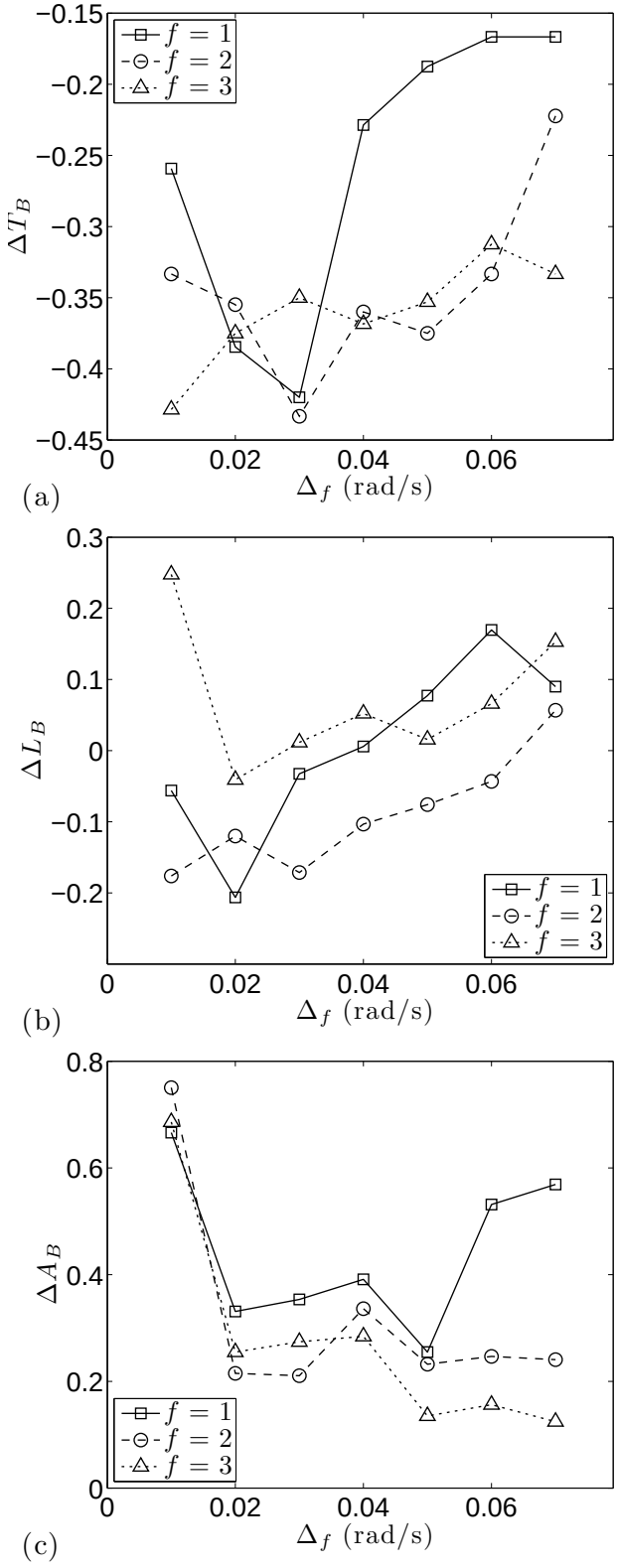

Figure 11. Relative error between our numerical and experimental calculations for (a) the time of wave breaking, (b) the breaking wave length, and (c) the breaking wave amplitude.